A long-term monthly surface water storage dataset for the Congo basin from 1992 to 2015

Benjamin Kitambo[1,2,3], Fabrice Papa[1,4], Adrien Paris[5,1], Raphael M. Tshimanga[2], Frederic Frappart[6], Stephane Calmant[1], Omid Elmi[7], Ayan Santos Fleischmann[8], Melanie Becker[9], Mohammad J. Tourian[7], Rômulo A. Jucá Oliveira[1], Sly Wongchuig[1]

[1]Laboratoire d'Etudes en Géophysique et Océanographie Spatiales (LEGOS), Université de Toulouse, CNES/CNRS/IRD/UT3, Toulouse, France
[2]Congo Basin Water Resources Research Center (CRREBaC) & the Regional School of Water~~, Department of Natural Resources Management~~,
University of Kinshasa (UNIKIN), Kinshasa, Democratic Republic of the Congo
[3]Faculty of Sciences, Department of Geology, University of Lubumbashi (UNILU), Route Kasapa, Lubumbashi, Democratic Republic of the Congo
[4]Institute of Geosciences, Campus Universitario Darcy Ribeiro, Universidade de Brasília (UnB), 70910-900 Brasilia (DF), Brazi
[5]Hydro Matters, 1 Chemin de la Pousaraque, 31460 Le Faget, France
[6]INRAE, Bordeaux Sciences Agro, UMR1391 ISPA, 71 Avenue Edouard Bourlaux, 33882 CEDEX Villenave d'Ornon, France
[7]Institute of Geodesy, University of Stuttgart, Germany
[8]Instituto de Desenvolvimento Sustentável Mamirauá, Tefé, AM, Brazil
[9]LIENSs/CNRS, UMR 7266, ULR/CNRS, 2 Rue Olympe de Gouges, La Rochelle, France

Correspondence to: Benjamin Kitambo (benjamin.kitambo@legos.obs-mip.fr)

Abstract. The spatio-temporal variation of surface water storage (SWS) in the Congo River basin (CRB), the second largest watershed in the world, remains widely unknown. In this study, satellite-derived observations are combined to estimate SWS dynamics at the CRB and sub-basin scales over 1992-2015. Two methods are employed. The first one combines surface water extent (SWE) from the Global Inundation Extent from Multi-Satellite (GIEMS-2) dataset and the long-term satellite-derived surface water height from multi-mission radar altimetry. The second one, based on the hypsometric curve approach, combines SWE from GIEMS-2 with topographic data from four global Digital Elevation Models (DEMs), namely The Terra Advanced Spaceborne Thermal Emission and Reflection Radiometer (ASTER), Advanced Land Observing Satellite (ALOS), Multi-Error-Removed Improved-Terrain (MERIT) and Forest And Buildings removed Copernicus DEM (FABDEM). The results provide SWS variations at monthly time step from 1992 to 2015 characterized by a strong seasonal and interannual variability with an annual mean amplitude of ~101 ± 23 km^3. Middle-Congo sub-basin shows higher mean annual amplitude (~71 ± 15 km^3). The comparison of SWS derived from the two methods and four DEMs shows an overall fair agreement. The SWS estimates are assessed~~evaluated~~ against satellite precipitation data and in situ river discharge and, in general, a relatively fair~~good~~ agreement is found between the three hydrological variables at the basin and sub-basin scales (linear correlation coefficient > 0.5). We further characterize the spatial distribution of the major drought that occurred across the basin at the end of 2005 and early 2006. The SWS estimates clearly reveal the widespread spatial distribution of this severe event (~~less than~~ ~40% deficit as compared to their long-term average~~of the mean maximum~~), in accordance with the large negative anomaly observed in precipitation over that period. This new SWS long-term dataset over the Congo basin is an unprecedented new source of information for improving our comprehension of hydrological and biogeochemical cycles in the basin. As the datasets used in our study are available globally, our study opens opportunities to

a mis en forme : Police :10 pt, Non Italique, Couleur de police : Noir

45 further develop satellite-derived SWS estimates at the global scale. The dataset of the CRB's SWS is available for download at https://doi.org/10.5281/zenodo.7299823 (~~k~~Kitambo et al., 2022b).

1 Introduction

Freshwater on Earth's ice-free land accounts for only ~1% of the total amount of water globally (Vörösmarty et al., 2010; Steffen et al., 2015; Cazenave et al., 2016; Albert et al., 2021). However, terrestrial freshwater is
50 essential to all human needs, ecosystem environments, and biospheric processes. Freshwater on land (excluding ice caps) is stored in various forms, including glaciers, snowpack, aquifers, root zone (upper few meters of the soil), and surface waters. The latter includes rivers, lakes, man-made reservoirs, wetlands, floodplains and inundated areas (Boberg, 2005; Zhou et al., 2016). All these continental components are permanently interacting with the atmosphere and oceans, exchanging energy and water fluxes (i.e., precipitation, evaporation, transpiration
55 of the vegetation, heat transfer, and surface and underground runoff) through horizontal and vertical motions, characterizing the global water cycle (Trenberth et al., 2007, 2011; Good et al., 2015; Cazenave et al. 2016). These exchanges and the associated storage variations of continental freshwater, specifically surface waters, are key players in the climate system and water resources variability as well as in the global biogeochemical and hydrological cycles (Chahine, 1992; de Marsily et al., 2005; Oki and Kanae, 2006; Shelton, 2009; Stephens et al.,
60 2020). For instance, despite their small surface coverage (~6% of the continents), wetlands and floodplains have a substantial impact on flood flow alteration, sediment stabilization, water quality, groundwater recharge, and discharge (Bullock and Acreman, 2003). The amount of water stored through large floodplains and wetlands is a key component to understand the exchange between the main river channel and the dissolved and particulate material (sediment and organic matter) (Melack and Forsberg, 2001; Ward et al., 2017). Furthermore, ~~they~~it also
65 acts as a regulator for basin hydrology owning to storage effects along channel reaches (Reis et al., 2017; Wohl, 2021). Additionally, the amount of water stored and flowing through surface water bodies influences the biogeochemical and traces gas exchanges and transport between the atmosphere land and the ocean (Richey et al., 2002; Raymond et al., 2013, Hastie et al., 2021).

Surprisingly, in spite of the importance of surface water storage (SWS), our current knowledge about its spatio-
70 temporal variability is still poorly known, especially at regional and global scales (Mekonnen and Hoekstra, 2016; Cooley et al., 2021). Therefore, there is a fundamental need for the quantification of the storage of surface freshwater on land (Alsdorf et al., 2003, 2007; Rodell et al., 2015; O'Connell, 2017).

Efforts have recently been devoted to measure SWS for large lakes, reservoirs, rivers, floodplains, and wetlands in large river basins using satellite-derived observations. Papa and Frappart (2021) provide an overview of the
75 recent advances in the quantification of SWS in rivers, floodplains, and wetlands from Earth observations, presenting several studies (e.g., Frappart et al., 2008, 2010, 2012, 2015, 2018; Papa et al., 2013, 2015; Becker et al., 2018; Tourian et al., 2018; Normandin et al., 2018; Pham-Duc et al., 2020) that characterize the variations in SWS changes in different large river basins. For instance, Frappart et al. (2012) used continuous multi-satellite observations of surface water extent and water level from 2003 to 2007 to monitor monthly variations of SWS in
80 the Amazon basin and the signature of the exceptional drought of 2005, when the amount of water in rivers and floodplains was found to be ~70% below its long-term average. Papa et al. (2013) developed a hypsometric curve approach to derive SWS variations by combining surface extent from the Global Inundation Extent from Multi-satellite (GIEMS; Prigent et al., 2007) and topographic data from the global digital elevation model from the

Advance Spaceborne Thermal Emission and Reflection Radiometer (ASTER). At the basin scale, they showed that the mean annual amplitude of the Amazon SWS is ~1 200 km^3 and contributes to about half of the annual terrestrial water change as detected by Gravity and Recovery Climate Experiment (GRACE) data (Papa et al., 2021).

Despite being the second largest river system in the world, both in terms of the drainage area and discharge to the ocean, the Congo River basin (CRB)'s SWS still remains widely unknown. CRB yet hosts extensive floodplains and wetlands such as the well-known Cuvette Centrale region, which stores a large amount of freshwater, playing a crucial role in the sediment dynamics of the river, as well as in the global carbon storage (Datok et al., 2020; Biddulph et al., 2021).

Crowley et al. (2006) estimated terrestrial (surface plus ground) water storage within the Congo Basin for the period of April 2002 to May 2006 using GRACE satellite gravity data. The result showed a significant seasonal (30 ± 6 mm of equivalent water thickness) and long-term trends, the latter yielding a total loss of ~280 km^3 of water over the 50-month period of analysis. Lee et al. (2011) determined the amount of water annually filling and draining the Congo main wetlands to 111 km^3. This was done by using a water balance equation combining several remotely sensed observations (i.e., GRACE, satellite radar altimeter, GPCP, JERS-1, SRTM, and MODIS). Richey et al. (2015) provided a groundwater stress assessment quantifying the relationship between groundwater use and availability in the world's 37 largest aquifer systems using GRACE data. The Congo Basin aquifer is characterized as low stress from the Renewable Groundwater Stress ratio. At the basin scale, Becker et al. (2018) further estimated the spatio-temporal variability of SWS by combining surface water extent from GIEMS and radar altimeter-derived surface water height of rivers at 350 virtual stations (VSs) from the Environmental Satellite (ENVISAT) mission over the period 2003-2007. They reported that the mean annual variations of the CRB's SWS was about 81 ± 24 km^3, contributing to $19 \pm 5\%$ of the annual variations of GRACE-derived terrestrial water storage. Recently, Frappart et al. (2021) proposed a densification of the network of VSs by including water elevation variations over the floodplains of the Cuvette Centrale and showed that SWS estimates can be much larger than when only VSs over the rivers are used. In parallel, PALSAR observations in InSAR acquisitions were used over the Cuvette Centrale of the Congo in combination to ENVISAT altimetry to establish relationships between water depth and surface water storage and derived absolute surface water storage change over 2002–2011 (Yuan et al. 2017).

Despite these efforts to characterize CRB's SWS, there is still a lot to unravel about the dynamics of SWS in the basin, leaving major questions open: What are the spatio-temporal dynamics of SWS over long-term period at CRB basin and sub-basins scales? How is these dynamics modulated by climate variability and what is the SWS behavior during exceptional drought events?

Earth observation is a unique means to answer these questions and is very useful for monitoring large drainage basin climate and hydrology where in situ information is lacking (Fassoni et al., 2021, Kitambo et al., 2021). Thus, in this study, we use two approaches to estimate, for the first time, the ~~unprecedented estimates of~~ spatio-temporal variations of CRB's SWS over the period 1992-2015. The first approach (Frappart et al., 2008, 2011, 2012, 2019) is based on the complementarity between the spatio-temporal dynamics of the surface water extent, and satellite-derived surface water height. The second approach relies on the methodology developed by Papa et al. (2013) using the relationships between elevation from digital elevation models and surface water extent~~area~~ variations, called the hypsometric curve approach, that enables the estimation of SWS changes.

Section 2 presents the study area. Section 3 describes the datasets and ~~s~~Section 4 the methodology used in this study. Section 5 is dedicated to results and validation. An assessment~~evaluation~~ is performed comparing the developed SWS with other independent datasets such as historic and contemporary river discharge and precipitation data. Section 6 presents an application case of the dataset in which~~. We investigate~~ the spatial distribution of the major drought that occurred across the basin at the end of 2005 and early 2006 is investigated. Section 7 presents the repository from~~on~~ which the SWS dataset can be accessed freely, and finally, ~~s~~Section 8 provides the conclusions and future perspectives.

2 Study area

The CRB (Fig. 1) represent the second largest freshwater system in the world, behind the Amazon basin, both in terms of drainage area (~3.7×10^6 km^2) and mean annual river discharge (40 500 m^3 s^{-1}) (Laraque et al., 2009, 2013). This large basin hosts the Earth's second-largest expanse of tropical forest, covering about 45% of its area and the world's largest tropical peat carbon storage (~28% of the total tropical peat carbon). The vast resources of the basin support the livelihoods of 80% of the riparian population (Verhegghen et al., 2012, Inogwabini, 2020; White et al., 2021; Crezee et al., 2022). The Congo River flows over 4 700 km from its source in the southeastern part of the Democratic Republic of Congo (DRC) to the Atlantic Ocean and its drainage area spans over nine countries, Central Africa Republic, Cameroon, Republic of the Congo, Angola, DRC, Zambia, Tanzania, Rwanda, and Burundi.

The CRB is generally divided into six main subbasins (Fig. 1) based on the physiography of the basin (Laraque et al., 2020): Lower-Congo (southwest), Middle-Congo (center), Sangha (northwest), Ubangui (northeast), Kasai (south-center), and Lualaba (southeast). The mean surface air temperature over the basin is estimated to be 25° C. The average rainfall is 2 000 mm yr^{-1} in the central part of the basin and decreases to 1 100 mm yr^{-1} away from the equator. While the peak annual potential evapotranspiration is ~1 500 mm yr^{-1} near the equator, it decreases northwards and southwards to less than 1 000 mm yr^{-1} (Sridhar et al., 2022).

The central part of the basin is characterized by an internal drainage basin and a large tropical rainforest, the Cuvette Centrale, where the river system is dominated by large wetlands and floodplains, with flat topography ~~and the predominance of three cover of the tropical rainforest~~ (Bricquet, 1993; Laraque et al., 2009, 2020). The hydrology of the CRB is also dominated by the presence of several lakes (Figure 1). The southeast Lualaba sub-basin contains the majority of them. In the highland of the Bangweulu region, there are several lakes characterized by small depths (less than 10 m) of which~~where~~ lake Bangweulu is the largest (~2 000 km^2) and is bordered on its east part by large wetlands (14 000 km^2) formed of large grassy swamps and floodplains. One can also find Lake Mweru (~4 413 km^2 and ~37 m depth) and Lake Mweru Wantipa with a smaller surface area (~1500 km^2). The Upemba depression contains a mosaic of lakes (e.g., Upemba Lake) and wetlands that can reach seasonally ~8 000 to ~11 840 km^2 in extent. The east part of the CRB hosts Tanganyika and Kivu Lakes. Tanganyika Lake, the second deepest (i.e., ~1 470 m) lake worldwide, contains a volume of ~18 800 km^3 and drains into the CRB system through the Lukuga River (Gasse et al., 1989; Runge, 2007; Harrison et al., 2016). In the south center region of the CRB, the Mai-Ndombe and Tumba Lakes are located in the Kasaï and Middle-Congo sub-basins, respectively.

3 Datasets

3.1 Multi-satellite-derived surface water extent

We used the estimates of surface water extent (SWE) derived from the Global Inundation Extent from Multi-Satellite (GIEMS-2) which~~, that~~ provides global coverage at monthly time step of different water bodies including wetlands, rivers, lakes at 0.25° (~27 km) spatial resolution at the Equator (on an equal-area grid, i.e., each pixel covers 773 km^2; Prigent et al., 2007, 2020). The dataset was developed by merging observations from different sensors, as described in Prigent et al. (2007) and Papa et al. (2010). The last version used in this study, spans over a long-term period from 1992 to 2015. For more details about the technique, we refer to Prigent et al. (2007, 2020).

Several studies such as Prigent et al. (2007, 2020), Papa et al. (2008, 2010, 2013) and Decharme et al. (2011) have been assessing the interannual and seasonal dynamics of the long-term SWE in different environments against several variables, such as the in situ river discharges, in situ and satellite-derived water level in rivers, lakes, wetlands, the total water storage from GRACE, and the satellite-derived rainfall. Recently, the characterization and evaluation of the 24-year SWE from GIEMS-2 have been conducted in the CRB against the in situ river discharge and water level and the performance gave satisfactory results (see Fig. 6 to Fig. 10 of Kitambo et al., 2022a for details on the characterization and the assessment of GIEMS-2 over the CRB).

3.2 Radar-altimetry-derived surface water height

Satellite radar altimetry provides a systematic monitoring of surface water height (SWH) of large rivers, lakes, wetlands, and floodplains at the virtual station (VS), defined as the intersection of a water body with the satellite theoretical ground track. The temporal variation of SWH is retrieved according to the repeat cycle of the satellite (Da Silva et al., 2010; Cretaux et al., 2017), cycle that varies from ten to twenty-seven days for current operational satellites. Several studies, including Frappart et al. (2006), Da Silva et al. (2010), Papa et al. (2010, 2015), Kao et al. (2019), Kittel et al. (2021), Paris et al. (2022), and Kitambo et al. (2022), to name a few, have been conducted in different river basins to validate SWH variations against in situ water levels. Results generally show a good capability of radar altimeter to retrieve SWH variability with uncertainties ranging from a few centimeters to tens of centimeters, depending on the acquisition mode of the satellite and the environment characteristics (Bogning et al., 2018; Normandin et al., 2018; Jiang et al., 2020; Kittel et al., 2021; Kitambo et al., 2022a).

Over CRB, Kitambo et al. (2022) used ~2300 VSs from different satellite missions and their pooling based on the principle of the nearest neighbor (located at a minimum distance of 2 km, see Da Silva et al., 2010; Cretaux et al., 2017) to generate long-term time series with records lengths ranging from 12 to 25 years records (Fig. 2d of Kitambo et al., 2022a). A thorough assessment and validation of these long-term satellite-derived surface water height at nine in situ gauge stations provided root mean squared error ranging from 10 (with Sentinel-3A) to 75 cm (with European Remote Sensing satellite-2) (see Table 2 of Kitambo et al., 2022a).

In the current study, the satellite-derived SWH used are the ones spanning the record period 1995-2015, acquired from three satellites missions, (1) European Remote Sensing-2 satellite (ERS-2), with observations spanning April 1995 to June 2003, (2) the Environmental Satellite (ENVISAT, hereafter named ENV), with observations spanning March 2002 to June 2012, and (3) the Satellite with ARgos and ALtiKa (SARAL/Altika, hereafter named SRL), from which we use observations from February 2013 to July 2016. All the three satellite missions have 35 days repeat cycle. These datasets were made available by the Centre de Topographie des Océans et de

l'Hydrosphère (CTOH, http://ctoh.legos.obs-mip.fr). They come from the Geophysical Data Records made available by space agencies. For ERS-2, land reprocessing was used (Frappart et al., 2016). These datasets were processed using either the Multi-mission Altimetry Processing Software (MAPS, Frappart et al., 2015b) or the Altimetry Time-Series software (Frappart et al., 2021b) to generate the time series of water level. Therefore, the generated 160 VSs cover the entire CRB (see Fig. S1, in supplementary materials) and a period of ~21 years. The southern-eastern portion of the basin, including Upemba and Bangweulu Lake regions, was not covered by the SWH VSs due to the simultaneous lack of data from the three aforementioned satellite mission. Over this region, missing data were replaced by the annual cycle computed using the altimetry-based water levels available during the study period.

3.3 Digital elevation model

We used four freely available global Digital Elevation Models (DEMs) (Table 2): (1) Advanced Spaceborne Thermal Emission and Reflection Radiometer (ASTER) version 3, (2) Advanced Land Observing Satellite (ALOS), (3) Multi-Error-Removed Improved-Terrain (MERIT), and (4) Forest And Buildings removed Copernicus DEM (FABDEM).

DEMs are divided broadly in two categories based on the specific topographic surfaces they represent, which are digital surface model (DSM) and digital terrain model (DTM). DSM refers to the upper surface of natural and built or artificial features of the environment such as buildings, man-made features, and trees, while DTM represents the elevation of the earth surface removed with all natural and built features, i.e., the bare-earth surface (Guth et al., 2021; Hawker et al., 2022). Among the DEMs used, ASTER and ALOS are classified as DSM. MERIT is closer to a DTM because of the removal of tree height bias but it is not a complete DTM (Yamazaki et al., 2017; Hawker et al., 2022) due to other artifacts such as man-made features. In this study, only FABDEM can be considered as DTM (Hawker et al., 2022).

Therefore, in order to remove the presence of tree bias in DSMs, we subtract from them the forest canopy height from a global dataset (Potapov et al., 2020). For that, the global canopy height dataset, ASTER and ALOS were all resampled to 90 m spatial resolution using the nearest neighbour resampling method.

a mis en forme : Police :Times New Roman, 10 pt, Couleur de police : Noir, Motif : Transparente

3.4 Global Forest Canopy Height

The global forest canopy height (available at https://glad.umd.edu/dataset/gedi/, last access ~~0~~17 May~~November~~ 202~~3~~2) is a global dataset developed by combining the Global Ecosystem Dynamics Investigation (GEDI) lidar forest structure measurement and Landsat analysis-ready data time series (Potapov et al., 2020). GEDI is a new spaceborne lidar instrument onboard the International Space Station collecting data on the vegetation structure since April 2019 (Dubayah et al., 2020a). The spatial resolution of the dataset is 30 m providing the global forest canopy height map for the year 2019 in WGS84 reference system. The dataset covers zones between 54°N and 52°S globally and then we use it over the CRB. For more details on the dataset, we refer to Potapov et al. (2020).

3.5 Lake water storage anomaly

~~Over the largest lakes of the CRB, we used time series of monthly water storage anomaly for Lakes Bangweulu, Kivu, Mweru, Tanganyika, Upemba (see Fig. 1 for their locations; Fig. S2 for their time series) by combining~~

~~time series of lake surface water extent and lake water level provided by the HydroSat database accessible at http://hydrosat.gis.uni-stuttgart.de/ (Tourian et al. 2022). By the availability of water extent and level estimates at two consecutive measurements epochs, the lake water volume anomaly is calculated under the assumption that the lake morphology is regular and has a pyramidal shape.~~

Over the largest lakes of the CRB, time series of monthly water storage anomaly for Lakes Bangweulu, Kivu, Mweru, Tanganyika, Upemba (see Fig. 1 for their locations; Fig. S2 for their time series) are estimated using surface water extent and water level time series obtained from HydroSat database (accessible at http://hydrosat.gis.uni-stuttgart.de/ [Tourian et al. 2022]). After collecting the simultaneous lake water area and height measurements, the empirical relationship between lake surface water level and area is developed. This model represents the bathymetry of the lake for the part which is captured by remote sensing observations. By assuming that the lake has a regular morphology and a pyramid shape between two consecutive measurement epochs, the lake water level-area-storage model is developed. Finally, time series of lake water storage anomaly are calculated using the developed model and lake water level or surface extent measurements.

a mis en forme : Police :(Par défaut) Times New Roman, 10 pt, Motif : Transparente

a mis en forme : Police :(Par défaut) Times New Roman, 10 pt, Motif : Transparente

a mis en forme : Police :(Par défaut) Times New Roman, 10 pt, Motif : Transparente

a mis en forme : Police :(Par défaut) Times New Roman, 10 pt, Motif : Transparente

3.6. Auxiliary data

3.6.1 In situ river discharge

We used the monthly time series of historical and contemporary observations of in situ river discharge located at the outlet of five sub-basins (see Fig. 1 for their locations and Table 2 for their characteristics) obtained from the Congo Basin Water Resources Research Center (CRREBaC, https://www.crrebac.org/), and from the Environmental Observation and Research project (SO-HyBam; https://hybam.obs-mip.fr/fr/, last access: ~~0~~17 May~~November~~ 2023~~2~~).

3.6.2 Rainfall

We used precipitation estimates from the Multi-Source Weighted-Ensemble Precipitation (MSWEP) Version 2.8 (V2.8). MSWEP is a global precipitation product with a spatial resolution of 0.1 ° at 3-hourly temporal resolution (also available at daily scale), covering the period from 1979 to present in near real-time. MSWEP precipitation estimates are derived by optimally merging multiple precipitation data sources, such as gauge, satellite, and reanalysis estimates (Beck et al., 2019a). The latest MSWEP version (V2.8) includes several changes compared to its previous version (V2.2). Among the major updates, in addition to near real-time (NRT) estimates, it also features new data sources that were defined based on their superior performances.

The historical MSWEP V2.8 considers i) one model-based precipitation product: European Centre for Medium-Range Weather Forecasts (ECMWF) ReAnalysis 5 (ERA5); ii) two satellite-based precipitation products: the Integrated Multi-satellitE Retrievals for GPM (IMERG) algorithm and the Gridded Satellite (GridSat) data; and iii) gauge observations from various sources: the Global Historical Climatology Network-Daily (GHCN-D), the Global Summary of the Day (GSOD) databases, and several national databases. On the other hand, MSWEP V2.8 NRT merges i) two model-based precipitation products: ERA5 and National Centers for Environmental Prediction (NCEP) Global Data Assimilation System (GDAS) Analysis; and ii) two satellite-based precipitation products: Global Satellite Mapping of Precipitation (GSMaP) and IMERG. MSWEP was globally and regionally assessed

and it exhibits realistic spatial precipitation patterns in frequency, magnitude, and mean (Beck et al., 2017; Beck et al., 2019b). MSWEP V2.8 is available via http://www.gloh2o.org.

3.6.3 Total Water Storage Anomaly from the Gravity Recovery and Climate Experiment mission

The Gravity Recovery and Climate Experiment (GRACE) is a joint NASA and German Aerospace Center (DLR) mission launched in March 2002 (Tapley et al., 2004) and, together with its successor GRACE Follow-On (GRACE-FO) launched in 2018 (Tapley et al., 2019), provides estimates of changes in water storage at the basin scale. For the analysis in this study, we used data from GRACE/GRACE-FO Mascon data available at http://grace.jpl.nasa.gov (Wiese et al., 2016,2018). The mascon data provides surface mass changes with a spatial sampling of 0.5 degrees in both latitude and longitude (Watkins et al., 2015). From this dataset, we obtained time series of Terrestrial Water Storage Anomaly (TWSA) over the CRB through area weighted aggregation of those grid cells in basins.

4 Methods

In order to estimate SWS variations over the CRB, two approaches are used (Figure 2): a) the multi-satellite approach following the methodology of Frappart et al. (2008, 2011) and b) the hypsometric curve approach following the methodology of Papa et al., (2013) and Salameh et al., (2017).

4.1 Multi-Satellite Approach

The multi-satellite approach (Fig. 2a) consists of the combination of the SWE and satellite-derived SWH over inland water bodies (rivers, lakes, reservoirs, wetlands, and floodplains), generally derived from radar altimetry over a common period of availability for both datasets (Frappart et al., 2008, 2011; Becker et al., 2018; Papa and Frappart, 2021). Therefore, this complementarity of multi-satellite observations offers the possibility to quantify SWS changes and water volume variations in a watershed. SWE and SWH used in this study are respectively from GIEMS-2 and the family of spaceborne radar altimeters with 35 days repeat cycle (hereafter ERS-2, ENV, and SRL). Their common period of availability is 1995-2015.
We summarize in the next sections the two-step methodology and, for more details, we refer to Frappart et al. (2008, 2011, 2012, 2019).

4.1.1 Monthly maps of surface water level anomalies

Monthly maps of water level anomalies of 0.25° spatial resolution referenced to the EGM2008 geoid are derived by combining GIEMS-2 and the combined long-term time series of ERS-2_ENV_SRL (1995-2015) satellite-derived water levels. For each given month of the water levels, these are linearly interpolated over the GIEMS-2 grid and the elevation of each pixel is provided with reference to a map of minimum surface water levels estimated over 1995–2015 using the principle of the hypsometric curve approach between SWH from radar altimetry and SWE from GIEMS-2 to take into account the difference of altitude in each cell area of GIEMS-2. (See Frappart et al., 2012 for more details).

a mis en forme : Police :Gras

a mis en forme : Police :(Par défaut) Times New Roman, 10 pt, Couleur de police : Noir, Motif : Transparente

a mis en forme : Police :(Par défaut) Times New Roman, 10 pt, Couleur de police : Noir, Motif : Transparente

a mis en forme : Police :(Par défaut) Times New Roman, 10 pt, Couleur de police : Noir, Motif : Transparente

a mis en forme : Police :(Par défaut) Times New Roman, 10 pt, Couleur de police : Noir, Motif : Transparente

a mis en forme : Police :(Par défaut) Times New Roman, 10 pt, Couleur de police : Noir, Motif : Transparente

a mis en forme : Police :(Par défaut) Times New Roman, 10 pt, Couleur de police : Noir, Motif : Transparente

a mis en forme : Police :(Par défaut) Times New Roman, 10 pt, Couleur de police : Noir, Motif : Transparente

a mis en forme : Police :(Par défaut) Times New Roman, 10 pt, Couleur de police : Noir, Motif : Transparente

a mis en forme : Police :(Par défaut) Times New Roman, 10 pt, Couleur de police : Noir, Motif : Transparente

a mis en forme : Police :(Par défaut) Times New Roman, 10 pt, Couleur de police : Noir, Motif : Transparente

a mis en forme : Police :(Par défaut) Times New Roman, 10 pt, Couleur de police : Noir, Motif : Transparente

a mis en forme : Police :(Par défaut) Times New Roman, 10 pt, Couleur de police : Noir, Motif : Transparente

a mis en forme : Police :(Par défaut) Times New Roman, 10 pt, Couleur de police : Noir, Motif : Transparente

a mis en forme : Ne pas ajuster l'espace entre le texte latin et asiatique, Ne pas ajuster l'espace entre le texte et les nombres asiatiques, Bordure : Haut: (Pas de bordure), Bas: (Pas de bordure), Gauche: (Pas de bordure), Droite: (Pas de bordure), Entre : (Pas de bordure)

4.1.2 Monthly time series of surface water storage variations

Following Frappart et al. (2012, 2019), the time variations of SWS are computed at the basin scale as

$$V_{SW}(t) = R_e^2 \sum_{j \epsilon S} P(\lambda_j,\varphi_j,t)(h(\lambda_j,\varphi_j,t) - h_{min}(\lambda_j,\varphi_j)) \cos(\varphi_j)\Delta\lambda\Delta\varphi \quad (1)$$

where V_{SW} is the volume of surface water, R_e is the radius of the Earth (6 378 km), $P(\lambda_j,\varphi_j,t)$, $h(\lambda_j,\varphi_j,t)$, and $h_{min}(\lambda_j,\varphi_j)$ are respectively, the percentage of inundation, the water level at time t, and the minimum of water level at the pixel (λ_j,φ_j), and $\Delta\lambda$ and $\Delta\varphi$ are respectively, the grid steps in longitude and latitude.

The maximum error on the volume variation is estimated as follows:

$$\Delta V_{SW,max} \leq \Delta S_{max}\delta h_{max} + S_{max}\Delta(\delta h_{max}) \quad (2)$$

where $\Delta V_{SW,max}$ is the maximum error on the water monthly volume anomaly, S_{max} is the maximum monthly flooded surface, δh_{max} is the maximum water level variation between two consecutive months, ΔS_{max} is the maximum error for the flooded surface, and $\Delta(\delta h_{max})$ is the maximum error for the water level between two consecutive months.

Note that the volume of SWS variations in a given basin is the sum of the contributions of the water storage contained in floodplains, wetlands, rivers, and small lakes. For larger lakes, as mentioned previously, estimates of SWS are complementarily obtained by the HydroSat database (Tourian et al. 2022). Therefore, the water storage analysis takes into account variations in floodplains, wetlands, rivers, and lakes.

4.2 Hypsometric Curve Approach Using Digital Elevation Models

In complement to the multi-satellite approach, we also used the hypsometric curve approach that consists of the combination of SWE and DEM-based topographic data. Following Papa et al. (2013), we summarize here the four-step process (Fig. 2b) to estimate SWS, using as example the combination of GIEMS-2 SWE and FABDEM topography resampled at 90 m:

4.2.1 Establishment of the hypsometric curve (area – elevation relationship)

~~(1)~~ For each GIEMS-2 pixel (Fig. 3; left column), we first derived the cumulative distribution function of elevation values within the corresponding FABDEM subset (Fig. 3; center column). For each GIEMS-2 pixel, over the CRB, this corresponds to ~95 000 elevation points falling within the satellite-derived SWE pixel, from which the hypsometric curve or curve of cumulative frequencies is established. It is equivalent to the distribution of elevation values in each 773 km^2 pixel (with 773 km^2 of flood coverage at the abscissa convert into percentage 100%) sorted in ascending order to represent an area – elevation relationship (Fig. 3; right column).

4.2.2 Correction of the hypsometric curve

~~(2)~~ To avoid the overestimation of SWS at the pixel level from the unrealistic amplitude, ~~T~~this~~e next~~ step corrects the behavior of the FABDEM hypsometric curve (Fig. 4) ~~to avoid overestimation of SWS at the pixel level~~. For

a mis en forme : Police :Gras
a mis en forme : Police :Gras
a mis en forme : Espace Après : 8 pt
a mis en forme : Police :Gras
a mis en forme : Espace Après : 8 pt

each GIEMS-2 pixel, the established area- elevation relationship enables us to derive the elevation amplitude (i.e., Similar to the amplitude of SWH) from the corresponding difference between the average annual minimum and the average annual maximum of SWE over the period 1992-2015. The mean maximum amplitude of SWH over the CRB varies between 1.5 to ~7.5 m (see Fig. 5 of Kitambo et al., 2022a). In most cases (~90% of GIEMS-2 pixels), the elevation amplitude derived from the difference between the average minimum and maximum provides values that satisfactorily match the range of the SWH amplitude. Often, these realistic values correspond on the FABDEM hypsometric curve to the percentage of flood coverage representing the main channel or floodplains (lower part of hypsometric curve) with a smooth increase of slope (as in Fig. 4a and g). However, Fig. 4 also points out that some elevation amplitudes (from ~10% of GIEMS-2 pixels) are above the range of 1.5 to ~7.5 m. These pixels therefore present unrealistic amplitude as compared to the range of previous findings over the CRB that can lead to the overestimation of SWS at the pixel level (Fig. 4c and d). Usually, these higher values are localized above 20% of flood coverage.

For this, following Papa et al. (2013), we propose a simple procedure to correct the behavior of FABDEM hypsometric curve exceeding the range of 1.5 to ~7.5 m of elevation amplitude. For each percent increment of flood coverage area, if the corresponding value of elevation belongs to a 5% window of 773 km^2 pixel (i.e., ~35 km^2) where the standard deviation (STD) of elevation is below 0.7 m threshold, the elevation value is kept. Conversely, if the elevation value corresponding to the percent increment of flood coverage belongs to a window in which the STD is above 0.7 m, the elevation value is replaced by the fitted value based on a simple linear regression analysis using the two previous elevation values of the hypsometric curve. For instance, a given elevation value corresponding to 8% of flood coverage belonging to a window with STD (i.e., calculated using values at 8, 9, 10, 11, and 12%) greater than 0.7 m, will be replaced by the fitted value calculated using the simple linear regression equation obtained from the values at 6 and 7%. The next STD will be computed with values of elevation at 9, 10, 11,12, and 13%, and so on.

Several attempts of correction with different STD values ranging from 0.3 to 1.1 m were performed (as shown in Fig. S3 as supplementary material) and the STD 0.7 m was chosen due to the realistic comparisons with the variations of surface water heights from altimetric VS. This value is also in agreement with the one chosen for the Amazon River basin (Papa et al., 2013).

Note that there is a non-significant percentage of pixels (~1%) for which, the hypsometric curve correction results in a slight increase of elevation amplitudes instead of a decrease (Fig. S4, in supplementary materials). However, these pixels generally provide acceptable estimates of SWS, without unrealistic overestimations.

Note also that, beside this correction, the hypsometric curve obtained from ASTER and ALOS showed roughness in their curve (Fig. S5, in supplementary materials), which was smoothed out using Savitzky-Golay filter embedded in SciPy API package in python before applying the correction described above.

4.2.3 Establishment of the area – surface water storage relationship

~~(3)~~ The hypsometric curve representing the area-elevation relationship is then converted into an area-SWS relationship by estimating the surface water storage associated with an increase of the pixel fractional open water coverage (with an increment of 1%) by filling the hypsometric curve from its base level to an upward level. Here we used three formulas for comparison purposes:

a mis en forme : Police :Gras

a mis en forme : Espace Après : 8 pt

$$V(\alpha) = \sum_{i=1}^{\alpha} (H_i - H_{i-1}) * S_i \quad (3)$$

$$V(\alpha) = \sum_{i=1}^{\alpha} (H_i - H_{i-1}) * \frac{S_i + S_{i-1}}{2} \quad (4)$$

$$V(\alpha) = \sum_{i=1}^{\alpha} \frac{(H_i - H_{i-1})}{3} * (S_i + S_{i-1} + \sqrt{S_i * S_{i-1}}) \quad (5)$$

where V is the surface water storage in km^3 for a percentage of flood inundation α. Note that the incrementation is on a step of 1%. S is the 773 km^2 area of GIEMS-2 pixel, and H represents the elevation (in km) for a percentage of flood inundation α given by the hypsometric curve.

Three formulas, (3), (4), and (5) used to retrieve the estimation of SWS from the hypsometric curve approach are compared in Figure 5. It shows that there is a slight difference in the SWS changes of about one hundredth after the decimal point between the three formulas (3), (4), and (5) except for Fig. 5d and g where the difference is of one-tenth after the decimal point. Overall, the difference seems negligible, and we decided to use only the formula (5) representing a volume of a trunk or regular truncated pyramid for SWS computation based on the hypsometric curve approach.

4.2.4 Monthly time series of surface water storage variations

~~(4) Finally, the hypsometric curve of the area-SWS relationship is combined with the monthly variations of SWE from GIEMS-2. This enables thus the estimation of SWS for each month by intersecting the hypsometric curve value with the GIEMS-2 estimates of pixel coverage for that month (Fig. 5). For each pixel, estimated SWS is subtracted by the minimum observed storage due to the fact that the water storage below the lowest levels of storage is not accessible, thus the incrementation starts above the minimum observed.~~

Finally, the hypsometric curve of the area-SWS relationship is combined with the monthly variations of SWE from GIEMS-2. This enables thus the estimation of SWS for each month by intersecting the hypsometric curve value with the GIEMS-2 estimates of pixel coverage for that month (Fig. 5). Note that with such method, the lowest level of storage refers to the level zero, determined by the minimum of SWE from GIEMS-2 observations for each pixel, from which the variation of the storage is started to be accounted for. Thus, the estimated SWS represents the increment above the minimum storage.

It is worth noting that, in the attempt of determining the extreme low storage values of exceptional drought years, it can be a potential source of uncertainties in a sense that DEM's values should have produced credible elevation data for those periods at the lower part of the hypsometric curve. Such information is unfortunately difficult to assess.

a mis en forme : Police :Gras

a mis en forme : Espace Après : 8 pt

a mis en forme : Police :(Par défaut) Times New Roman, 10 pt, Non Italique

a mis en forme : Interligne: 1,5 ligne

a mis en forme : Police :(Par défaut) Times New Roman, 10 pt, Non Italique,Couleur de police : Noir

a mis en forme : Police :10 pt, Non Italique,Couleur de police : Noir

a mis en forme : Police :(Par défaut) Times New Roman, 10 pt, Non Italique

5 Results and validation

5.1 Distribution and variability of surface water storage across the Congo River basin

Figure 6 presents the characteristics of the SWS temporal dynamics at CRB scale (anomaly time series versus its long-term mean, deseasonalized anomaly, and annual cycle for SWS aggregated for the entire CRB). It shows all SWS estimates computed with both the multi-satellite (for 1995-2015) and the hypsometric curve (for 1992-2015) approaches from the use of the four DEMs (ALOS, ASTER, MERIT, and FABDEM).

Figure 6a shows, for the very first time, the long-term month-to-month variations of the CRB's SWS over a period of 24 years. It shows a strong seasonal cycle of SWS over the CRB showing a comparable behavior in the peak-to-peak SWS variations from both approaches. The SWS amplitude ranges from ~50 to ~150 km^3 over the years, showing a large year-to-year variability. The bi-modal patterns that characterizes the hydrological regime of the CRB's (Kitambo et al., 2022a), linked to the variability of the intertropical convergence zone (Kitambo et al., 2022a), is well depicted in the SWS estimates.

All SWS estimates from the different DEMs show fair agreement in their variations in between them (Fig. 6a). However, we observed that SWS from ASTER (violet color) tends to overestimate the SWS at the first peak (i.e., spanning over August-February) along the time series.

Figure 6b displays the deseasonalized anomaly (obtained by subtracting the mean monthly values over the considered period, 1992-2015, or 1995-2015 from individual months) of CRB's SWS. A similar observation about the matching of SWS anomaly from different approaches and DEMs products is observed.

These SWS estimates also show a substantial interannual variability at basin scale, especially in terms of annual maximum and minimum, pointing out extreme events in terms of droughts and floods that recently affected the CRB. Figure 6b reveals interesting and strong anomaly signals such as the large positive peaks observed in 1997-1998 and 2006-2007. These can be related to the positive Indian Ocean Dipole (pIOD) events, in combination with the El Niño events that occurred in 1997–1998 and 2006–2007 that triggered floods in western Indian Ocean and eastern Africa (Mcphaden, 2002; Ummenhofer et al., 2009; Becker et al., 2018, Kitambo et al., 2022a). Another major event is the severe drought that occurred in 2005-2006 that is clearly depicted on the CRB's SWS time series anomaly as the minima of the record (Fig. 6b). This is in agreement with Ndehedehe et al. (2019, 2022) and Tshimanga et al. (2022) who reported that, in the 1990s and 2000s's, multi-year droughts in the CRB affected a significant part of the Congo basin. This interannual variability is also superimposed to variations at larger time scale, from few years to decadal, such as a large increase in SWS anomaly in 1996-1997, followed by a slight decrease until the minimum that occurred in 2005-2006, before SWS starts to slowly increase again after the 2007 peak, until 2015.

Figure 6c shows the CRB's SWS annual cycle (computed over 1992-2015 and 1995-2015 period for the hypsometric and multi-satellite approaches, respectively) revealing a strong seasonal variation. Both approaches present a mean annual amplitude of the same order in magnitude (Table 3) with estimates ranging around 80 ± 17, 101 ± 23, 80 ± 20 km^3 (respectively from ALOS, FABDEM and MERIT based on the hypsometric curve approach), and 70 ± 17 km^3 from the multi-satellite approach. These estimates are of the same order of magnitude with previous findings over the CRB, i.e., 81 ± 24 km^3 as in Becker et al. (2018). As a matter of comparison, the mean annual amplitude of SWS from ASTER represents ~11% of the Amazon basin's SWS mean annual amplitude of ~1200 km^3, as reported in Papa et al. (2013, 2021).

As observed in Fig. 6a, ASTER's SWS provides larger estimates, with a mean annual amplitude of ~124 ± 25 km^3 (Table 3). This can be explained by the fact that, among the four DEMs (ALOS, ASTER, FABDEM and MERIT), ASTER has a greater vertical error (i.e., 17 m, see Table 1 of Hawker et al., 2019) compared to the others and, consequently, this can impact the elevation amplitude (derived at step 2 of section 4.2 used to calculate the SWS variations (step 3 of section 4.2).

Table 3 presents also the statistics errors comparing the FABDEM's SWS dataset to other estimates and reinforce the difference highlighted in SWS magnitude between different approaches and DEMs. Note that trees and urban areas biases are only removed from FABDEM, and thus it seems to be the most adequate DEM in representing hydrology processes (Hawker et al., 2022). ALOS and MERIT have provided small errors as reflected in the mean absolute error (MAE) (9 and 5 km^3) and the root mean squared error (RMSE) values (11 and 7 km^3) compared to values greater than 15 km^3 of MAE and above 20 km^3 of RMSE from multi-satellite approach and ASTER DEM. At the basin scale, Fig. 6c clearly depicts a double peak, with a SWS maximum reached in November for the first peak and in April for the second peak. In comparison with the annual cycle of GIEMS-2 SWE (Fig. 7c of Kitambo et al., 2022a), the first peak of SWS maximum is in phase with the maximum SWE, while for the second peak there is a one-month delay, with maximum SWE occurring in March. This can be explained by the non-linear relationship between SWE and SWS through the hypsometric curve approach.

It is important to note that SWS from FABDEM and MERIT shows a very good fit at all seasons whereas ALOS slightly underestimates the storage at the second peak. Contrary to others, ASTER shows a peculiar behavior with its SWS largely underestimating and overestimating the storage at the second and first peak of the hydrological regime, respectively.

In agreement with the results from the SWS hypsometric curve approach, SWS from the multi-satellite approach also points out the maximum SWS in November and April for the first and second peaks. However, the dynamics of SWS from the multi-satellite approach differs from the others over the period from February to May. Over that period of time, the hydrological regime of the basin is more controlled by the southeast region, especially by the Bangweulu and Upemba Lake area (Kitambo et al., 2022a). In this region, the spatial distribution of VSs is not sufficient enough (Fig. S1, in supplementary materials) to obtain a very accurate representation of the temporal variations of the SWS even if the mean annual cycle variations of some VSs from ENV and SRL were used to account for the water level over the entire 1995-2015 period. This might explain in part the different dynamics observed in the SWS variations over February-May in the southeastern region.

In parallel to Fig. 6, Fig. 7 presents the spatial distribution of SWS dynamics (mean annual, Standard Deviation (STD), mean annual maximum, and average month of the maximum) for the entire CRB. In the following parts of the paper, the estimates obtained with the FABDEM DEM will become our reference and we will use them to display the results. This is justified by FABDEM DEM topographic characteristics and properties which makes it the closest to a DTM. The estimates obtained with the other DEM will be displayed in Supplementary Material (Fig. S6).

In agreement with the spatial distribution of SWE across CRB (Fig. 6 of Kitambo et al., 2022a), SWS (Fig. 7a and b) shows realistic spatial patterns along the Congo River and the Cuvette Centrale and depict quite well the other main structures of the basin, for instance, the main tributaries (e.g., Sangha, Ubangui, Luvua, Luapula, Lualaba Rivers) along with their large wetlands and floodplains. These are characterized by a strong variability in SWS (Fig. 7c and d).

Higher values of SWS ranging from 0.3 to 0.6 km^3 in a 773 km^2 dominate the extensive wetlands and floodplains such as the Cuvette Centrale and in the southeastern part of the basin (Upemba and Bangweulu region). These regions display a large variability as well (in terms of the STD, Fig. 7c and d) and are characterized by maximum values of surface water storage generally greater than 0.6 km^3 per pixel of 773 km^2 (Fig. 7e and f).

The heart of the Cuvette Centrale as well as the lake Mai-Ndombe (in the Kasai sub-basin) and a large part of the main channel of the Congo (up to Lomami River) present the maximum values of the SWS change in the basin. Same observation is done for the lakes in the Upemba depression (e.g., Upemba Lake), Mweru and Bangweulu. These maximum values are reached in September-October in the upper part of the Cuvette Centrale and November-December in their lower part (Fig. 7g and h). In the Lualaba sub-basin, the average month of the maximum of SWS is January-February, while in other parts, such as lake Mweru and the east part of Bangweulu, with its large grassy swamps and floodplains, it recorded in March-April. Conversely to the general trend in the Cuvette Centrale, the region of lake Tumba and Mai-Ndombe reached their maximum of SWS in July-August.

In general, the results from the hypsometric curve (Fig. 7, left column) and multi-satellite (Fig. 7, right column) approaches are quite similar in terms of spatial distribution, for both magnitude and variability of the changes. Nevertheless, as expected, the multi-satellite dataset approach shows a limitation in terms of spatial distribution caused by the reduced availability of the combined long-term VSs in some regions. For instance, there is a lack of observations on the east part of the Tanganyika Lake and in the Bangweulu region, where the spatial distribution of SWS from the multi-satellite approach is smaller than that of the FABDEM hypsometric curve approach. This is mainly explained by the sparse availability of long-term satellite-derived (ERS2-ENV-SRL) time series in that region, leading to less distributed SWS estimates in these regions.

On the other hand, SWS variations from hypsometric curve approach also present limitations, mainly on small lakes and around large lakes where there are almost no variations in elevation from the DEMs leading to flat hypsometric curves, and therefore to the computed storage to be of zero changes. This is for instance the case around Lake Kivu in the Lualaba sub-basin. In this case, the SWS change of the lake is then added to the dataset using the Lake Water Storage Anomaly computed independently (see Data description in section 3.5).

Finally, for comparison purposes, Fig. S6 (in supplementary materials) shows the same analysis in terms of spatial distribution and variability of SWS across the basin for the other estimates based on the hypsometric curve approach (i.e., ALOS, see Fig. S6 left column; ASTER, see Fig. S6 middle column; and MERIT, see Fig. S6 right column). In general terms, results are consistent between one another. The pattern of SWS in terms of the distribution and order of magnitude of the mean annual (Fig. S6a, b, and c), variability in terms of STD (Fig. S6d, e, and f), mean annual maximum (Fig. S6g, h, and i) and average month of the maximum (Fig. S6j, k, and l) between the three DEMs and FABDEM are generally similar although results from ASTER DEM (Fig. S6b, e, and h) underestimate the storage (i.e., values ranging between 0.15-0.45 km^3) compared to other DEMs (i.e., values greater than 0.6 km^3) in the Bangweulu-Upemba region (e.g., Lake Bangweulu, Lake Upemba).

At the sub-basin scale, the mean annual amplitude for the five sub-basins is provided as follows. Middle-Congo is the sub-basin with the large amplitude (71 ± 15 km^3), associated with the strong variations of SWS anomaly observed in the Cuvette Centrale. It is followed by Lualaba sub-basin with 59 ± 15 km^3 due to the presence of major lakes (Kivu, Tanganyika, Mweru, Bangweulu) and large wetlands that show large variability and are characterized by maximum values of surface water storage generally greater than 0.6 km^3 per pixel of 773 km^2. Sangha and Kasaï show quite similar annual amplitude (i.e., respectively of 24 ± 5 and 24 ± 6 km^3). Both sub-basins are overlapped at their mouth (i.e., downstream part) by the Cuvette Centrale. Among the five sub-basins, Ubangui is the one with the smallest mean annual amplitude (13 ± 4 km^3) although it is among the two northern sub-basins (i.e., Ubangui and Sangha) with higher satellite-derived SWH mean maximum amplitude (see Fig. 5a

of Kitambo et al., 2022a). As observed for Sangha and Kasaï subbasins, Ubangui subbasin is also occupied by its downstream part by the Cuvette Centrale (Fig. 1).

5.2 Evaluation against independent datasets

In order to evaluate the monthly estimates of the large-scale SWS over the CRB, we compare, at the basin and sub-basin levels, their seasonal and interannual variability against other independent hydrological variables such as precipitation data from MSWEP V2.8 and in situ discharges. For clarity purpose, only the SWS result from the hypsometric curve approach with FABDEM and from the multi-satellite approach are displayed and discussed here.

At the basin level, Fig. 8 presents the comparison of the aggregated normalized SWS anomaly variation over the entire basin against the normalized precipitation anomaly and the in situ normalized discharge anomaly at the outlet of the basin (Brazzaville/Kinshasa station, see Table 2). The normalized anomalies here are estimated by subtracting the mean value of the time series from individual months and by dividing the obtained series by the STD of the original time series). As a complement, we report in Table 4, the maximum linear Pearson correlation coefficient, along with their lag, calculated between the aggregated normalized SWS anomaly variation, the normalized precipitation anomaly, and the in situ normalized discharge anomaly, at basin and sub-basin scales. Figure 8a presents a fair agreement between the SWS and the other two hydrological variables, with a maximum correlation coefficient r of 0.56 (lag = 0; p value < 0.01) between SWS and precipitation variations. A similar correlation coefficient (r = 0.57 with a 0-month lag; p value < 0.01) is found between normalized SWS anomaly and in situ normalized discharge anomaly. The deseasonalized normalized anomaly (acquired by subtracting the mean monthly values over the considered period, 1992-2015 or 1995-2015 from individual months and dividing by the STD of the raw series) (Fig. 8b) show correlation coefficient of r = 0.52 (lag = 0; p value < 0.01) and r = 0.12 (lag = 0; p value < 0.05) respectively between SWS versus in situ discharge and SWS versus precipitation. Additionally, we also perform a comparison with previous estimates of SWS over the Congo basin from Becker et al. (2018), estimated using the multi-satellite approach and available over the period 2003-2007. The assessment with SWS anomaly from FABDEM shows a good agreement (Fig. 8a), with similar amplitude, with a maximum correlation coefficient of r = 0.73 (lag = 0; p value < 0.01).

At the seasonal time-scale, Fig. 8c reveals for the first peak (i.e., August-February) that SWS anomaly reaches their maximum in November, one month before the maximum of the river normalized discharge anomaly (December) and after the maximum of normalized precipitation anomaly data (October). Same observation is made in terms of the temporal shift for the second peak (i.e., March-July), where the maximum of SWS anomaly occurs in April and one month later for normalized discharge anomaly and one month before for normalized precipitation anomaly respectively in May and March.

Figure 9 displays the comparison at the basin level between the aggregated normalized SWS anomaly and TWSA from GRACE. Both variables, show a similar interannual variability during the common period of availability of data (i.e., 2002 to 2015) presenting a fair correlation of r = 0.84 (lag = 1; p value < 0.01; Fig. 9a). It is worth to mention as well that both datasets capture the bi-modal patterns. Figure 9b presents the deseasonalized normalized anomaly for the two variables (r = 0.4; lag = 0; p value < 0.01), showing quite similar variations, especially in the long-term variability. We also notice the higher magnitude of the normalized SWS anomaly as compared to the normalized TWSA. At the seasonal time-scale, Fig. 9c reveals a similar behavior, with the two peaks depicted in

a mis en forme : Police :10 pt, Non Italique, Couleur de police : Noir

the two variables, one in November-December and one in April. The lowest level of the SWS happens in July that is one month ahead of TWSA minimum.

Figure 10~~9~~ presents the same comparison as done in Fig. 8 but at the sub-basin level (considering Ubangui, Sangha, Middle-Congo, Kasaï, and Lualaba sub-basins, see Fig.1). The seasonal variations of all sub-basins are provided in Fig. 10~~9~~ (right column). The outlet of Kasaï and Lualaba sub-basins provides historical observations (i.e., data before the 1990s), thus, the comparison with its in situ normalized discharge anomaly time series was integrated only at the annual cycle. For Ubangui, Sangha, and Lualaba sub-basins, the maximum linear correlation coefficient is not significant between normalized SWS anomaly and normalized precipitation anomaly variations at the interannual level and their associated anomaly (Figs. 10~~9~~a, b, d, e, m, and n, Table 4). This could be associated to the bi-modal dynamics observed in the precipitation data whereas the SWS variations do not show that behavior. Becker et al. (2018), using similar datasets (GIEMS-1 for SWE and VS from ENVISAT), reported the same observation between precipitation data with a bi-modal patterns and SWE with uni-modal patterns (Fig. 4 of Becker et al., 2018). Another reason could be that, for Ubangui and Sangha, SWS is mainly function of discharge variations, while for the Lualaba sub-basin, that encompasses many lakes and floodplains, the various processes and their link for instance with evaporation lead to an insignificant precipitation-SWS correlation. Additionally, one can observe a negative lag between normalized SWS anomaly and normalized precipitation anomaly for Ubangui and Lualaba sub-basins which is not physically acceptable since we except positive temporal shift between SWS and precipitation. This is probably due to the fact that SWS show uni-modal pattern while precipitation shows bi-modal pattern. Nevertheless, the comparison between normalized SWS anomaly versus normalized discharge anomaly for Ubangui and Sangha, except for Lualaba sub-basin, shows fair correlation coefficient ($r > 0.7$; p value < 0.01) at the interannual time-scale (Fig. 10~~9~~a and d). Their related deseasonalized normalized anomalies (Fig. 10~~9~~b and e) presents lower values of correlation coefficients ($r < 0.4$; p value < 0.01). Regarding Middle-Congo and Kasaï subbasins (Fig. 10~~9~~g and j), a maximum linear correlation coefficient is respectively of $r = 0.32$ and $r = 0.69$ (lag = 0; p value < 0.01) between normalized SWS anomaly and normalized precipitation anomaly. Their associated deseasonalized normalized anomaly (Fig. 10~~9~~h and k) does not show significant correlation coefficient. In contrast to this, for Middle-Congo, the comparison between SWS and discharge provides moderate correlation coefficient for both interannual and deseasonalized anomaly variations ($r > 0.5$ with a delay lag of 1-month; p value < 0.01). In accordance with other results (see Fig. 10h of Kitambo et al., 2022a), the Middle-Congo appears to be the main sub-basin for which the variability of the normalized discharge anomaly at the outlet Brazzaville/Kinshasa station is fairly related (~35%) to the variations of normalized SWS anomaly in the Cuvette Centrale region due to its significant correlation coefficient of $r = 0.58$ between the deseasonalized normalized anomaly of both SWS and discharge. Northern and the Middle-Congo sub-basins reach their SWS anomaly' maximum in November (for Sangha and Middle-Congo, fig. 9f and i) and October (for Ubangui, Fig. 10~~9~~c), and this is in phase with the maximum of the normalized discharge anomaly and a backward temporal shift of 1 month with the normalized precipitation anomaly. Comparatively to northern sub-basins, southern sub-basins (Kasaï and Lualaba), for the period January to May, reach their SWS anomaly' maximum in March (Fig. 10~~9~~l and o) that is in phase with the occurrence of the maximum of normalized precipitation anomaly. The maximum of normalized discharge anomaly occurs two months later in May for Lualaba and one month later for Kasaï. In contrast to the other sub-basins, Kasaï and Middle-Congo have depicted the bi-modal patterns in SWS anomaly variations. For Middle-Congo, the first peak is reached in November and

the second in May while for Kasaï, the first peak occurs in December and the second peak with a steadily evolution occurs in March and May. Similar results were observed in the Cuvette centrale by Frappart et al. (2021a).

The temporal patterns in Fig. 8 and 10~~9~~ follow alternatively wet and dry events associated with large-scale climatic phenomena, for all dataset (SWS, precipitation and discharge). A focus on the Lualaba and Kasai deseasonalized normalized anomaly of SWS reveals that there are the two main sub-basins significantly impacted (large positive anomaly in Fig. 10~~9~~k and 10~~9~~n) by the major flood event triggered by the positive Indian Ocean Dipole in combination with the El Niño event that characterized the period 1997-1998. Conversely, recent studies using hydro-meteorological datasets have shown that some parts of the CRB are subjects to a long-term drying trend over the past decades (Hua et al., 2016; Ndehedehe et al., 2018). The droughts that affected large areas of CRB in recent years are amongst the most severe ones in the past decades (Ndehedehe et al., 2022), including the large anomalous event of the 2005-2006 drought (Fig. 8). This is further investigated below.

6 Application: the spatio-temporal dynamics of SWS during the 2005-2006 drought

SWS estimates are essential in the characterization of large-scale, extreme climate events such as droughts and floods (Frappart et al., 2012; Pervez and Henebry, 2015, Papa et al., 2021). Here, we investigated the spatial signature and distribution of the major drought that occurred in the end of 2005 and early 2006 across the CRB (Ndehedehe et al., 2019, 2022). During that period, SWS anomaly was at its lowest level at basin-scale (Fig. 6b). The spatial patterns of this drought are further illustrated in Fig. 1 10~~9~~ using the FABDEM estimates. The anomaly of SWS from FABDEM in the end 2005 and early 2006 is estimated here by subtracting the November-December-January mean values over 1992-2015 from the maximum value between November 2005 to January 2006 and by dividing the obtained value by the November-December-January mean values.

Figure 1 10~~9~~ evidences that during that period the major part of the basin was affected by large negative anomalies of SWS, with values sometimes reaching a 50% deficit as compare to their long-term average. It clearly shows a widespread severe drought across the basin (< - 40% of the mean maximum), even if some parts of the Oubangui sub-basin and Lukenie Rivers in the north of Kasaï sub-basin are relatively less affected (> - 10% of the mean maximum of SWS). Figure 1 10~~9~~ shows the large drought spatial signature of the southeastern wetlands/floodplains (e.g., Bangwelo, Upemba) in the Lualaba sub-basin, with SWS estimated at more than -40% of the mean maximum during that period. Notably, the heart of the Cuvette Centrale displays a stronger negative signal in terms of SWS. The hydrological dynamic in the Cuvette Centrale might explain that the mainstream that receives water from all adjacent wetlands and streams experiences a less intense impact of drought (Lee et al., 2011). This aligns with the previous findings that large parts of the CRB found to be extensively affected (Ndehedehe et al., 2019) and it is confirmed by analyzing the monthly mean spatial distribution of MSWEP precipitation anomaly (Fig. 12~~1~~) around that period of time. Figure 12~~1~~ shows the monthly mean spatial distribution of MSWEP precipitation anomaly at 0.25° spatial resolution from the period September 2005 to February 2006 based on the 1992-2015 climatology. Over the six months, November 2005 to January 2006 are the most impacted months (Fig. 12~~1~~c, d, e). November 2005 (Fig. 12~~1~~c) displays a large spread negative anomaly all over the basin whereas December 2005 (Fig. 12~~1~~d) and January 2006 (Fig. 12~~1~~e) show severe negative anomalies only in the southern part of the basin, in accordance with the spatial distribution of SWS across the basin as described previously. However, some parts of the Oubangui sub-basin and Lukenie Rivers in the north of Kasaï sub-basin seem to be

relatively less affected by the drought in terms of SWS, even if large precipitation negative anomaly is observed of these regions. Investigating the climatic and hydrological drivers of these anomalous events in CRB is far beyond the scope of the present study, but our results point out to the capability of this new long-term estimates of SWS to be used in future studies.

7 Data availability

The SWS estimates from the multi-satellite approach (1995-2015), as well as the hypsometric curves approach providing the surface water extent area-height relationships from the four DEMs (before and after the corrections), the surface water extent area-storage relationships, along with the four SWS estimates (1992-2005) are publicly available for non-commercial use and distributed via the following URL/DOI: https://doi.org/10.5281/zenodo.7299823 (Kkitambo et al., 2022b).

8 Conclusions and perspectives

In this study, we present an unprecedented dataset of monthly SWS anomaly of wetlands, floodplains, rivers and lakes over the entire Congo basin during the 1992-2015 period at ~ 0.25° spatial resolution. Two methods are employed, one based on a multi-satellite approach and one on a hypsometric curve approach. The multi-satellite approach consists of the combination of SWE from GIEMS-2 and satellite-derived SWH from radar altimetry (long-term series ERS-2_ENV_SRL) on the same period of availability for the two datasets, here 1995-2015. The hypsometric curve approach consists of the combination of SWE from GIEMS-2 dataset and hypsometric curves obtained from various DEMs (i.e., ASTER, ALOS, MERIT, and FABDEM). Both methods generate monthly spatio-temporal variations of SWS changes across the entire CRB, enabling for the first time the quantification of surface freshwater volume variations in the Congo basin over a long-term period (24-year). The SWS computed from different approaches, multi-satellite and hypsometric curve, and from different DEMs (ALOS, ASTER, MERIT, FABDEM), generally show good agreements between them at the interannual and seasonal scale, with minor exceptions for SWS variations from ASTER DEM due possibly to its largest vertical error. SWS variations from the multi-satellite approach show some limitations due to the spatial distribution of altimetry-derived VSs over the basin. The two approaches are complementary: the hypsometric curve approach allows to generate the SWS changes over the entire basin with limitation over lakes and in high altitude topography, while the multi-satellite one can generate SWS variations over lakes but with a spatial constraint on the availability of VSs. SWS variations from FABDEM, which is the only DTM among all the DEMs used (i.e., both biases associated with trees and building have been removed) is then used to illustrate the capability of the new dataset.

The temporal variations of SWS satisfactorily depicted the bimodal pattern at the interannual and seasonal scales, a well-known characteristic of the hydrological regime of the Congo basin. The mean annual amplitude was determined to be 101 ± 23 km^3, which, in perspective, represents ~8% of the Amazon basin's mean annual amplitude. The spatial distribution of the SWS has shown a realistic pattern for major tributaries of the Congo basin and its analysis showed large SWS variability (e.g., 0.3 to 0.6 km^3) over the extensive wetlands and floodplains such as the Cuvette Centrale and in the southeastern part (i.e., Bangweulu, Mweru, Upemba) of the basin. In the Cuvette Centrale, the maximum SWS values are reached in September-October in the upper part and in November-December in the lower part. The new monthly surface water storage has been compared on common period to the previous estimates over 2003-2007 showing a good agreement and a fair correlation coefficient.

Furthermore, an evaluation was conducted with independent hydrological variables, precipitation from MSWEP dataset and in situ discharges from contemporary and historical observations, showing an overall good correspondence among all variables. The estimates of SWS variations also enable to depict the major anomalous events related to droughts (e.g., exceptional drought documented in 2005-2006) and floods (e.g., exceptional flood occurred in 1997-1998). We further map, across the basin, the spatial signature of the widespread drought that took place in the end of 2005 and the beginning of 2006, revealing the severity of this particular event on surface freshwater store, in agreement with satellite-derived precipitation observations, although the northeast of the Cuvette Centrale and some tributaries of the Kasaï River (in the Mai-Ndombe Lake region) were less impacted. These unique long-term monthly time series of CRB's SWS provide the broad characteristic of the variability of surface water storage anomaly at the basin and sub-basin levels over 24-year in the CRB. It opens new perspectives to move toward answering several crucial scientific questions regarding the role of SWS dynamics into the hydrological and biogeochemical cycles of CRB. For instance, SWS estimates are a relevant source of information to make progress in the understanding of the hydrodynamic processes that drive the exchanges between rivers and floodplains, both in terms of freshwater and dissolved and particulate materials. Such datasets also enable us to explore the link between regional climate variability and water resources, especially during extreme events, and can now be used to improve our understanding of hydroclimate processes in the Congo region (Frappart et al., 2012).

Overall, these results from satellite-based observations also confirm the capability and benefits of using Earth observations in a sparse gauged basin such as the CRB to better characterize and improve our understanding of the hydrological science in ungauged basins. The information derived from SWS will therefore be very pertinent as a benchmark product regarding the calibration/validation of the future hydrology-oriented Surface Water and Ocean Topography (SWOT) satellite mission, ~~to be~~ launched ~~at the end of~~ on the 16th of December 2022, which will provide water storage variability of water bodies globally (Biancamaria et al., 2016). Additionally, SWS estimates provide a unique opportunity for future hydrological or climate modeling and to evaluate regional hydrological models (Scanlon et al., 2019) that still lack proper representation of surface water storage variability at large scale (Paris et al., 2022), especially in major African river basins (Papa et al., 2022).

Following previous studies (Frappart et al., 2019, Becker et al., 2018), SWS estimates also open new opportunities to generate a long-term spatio-temporal variations of sub-surface freshwater through decomposition of the Total Water Storage variations as measured by the GRACE/GRACE-FO (Gravity Recovery and Climate Experiment Follow-On) (Pham-duc et al., 2019). Such understanding of freshwater variations in the continental reservoirs has many potentials to better characterize the hydro-climate processes of the region and improve our knowledge on the water resources availability in CRB. For instance, SWS estimates are key to determine the total drainable water storage of a basin (Tourian et al., 2018, 2022), that provide essential information about the distribution and availability of freshwater in a basin.

Finally, since GIEMS-2 and the DEMS used in this study are available globally, our results thus present also a new first step toward the development of such SWS databases at the global scale. Furthermore, the proliferation of new DEMs that are proper DTMs, and the increasing availability of high-accuracy bare-earth DEMs (O'Loughlin et al., 2016; Yamazaki et al., 2017; Hawker et al., 2022) has opened new opportunities to better investigate SWS dynamics at the global scale. As highlighted in Papa and Frappart (2021), global SWS estimates and variations are crucial to understand the role of continental water in the global water cycle and global estimates

a mis en forme : Exposant

will offer new opportunities for hydrological and multidisciplinary sciences, including data assimilation, land–ocean exchanges and water management.

Author contributions BK, FP, AP, RTM, and SC conceived the research design. BK processed the data and created the SWS dataset from hypsometric curve approach. FF created the SWS dataset from multi-satellite approach. OE created SWS of lakes. RJO provided precipitation data and Figure 11. BK, FP, and AP analyzed and interpreted the results and wrote the draft. FP and RTM were responsible for the data curation. All authors discussed the results and contributed to the final version of the paper.

Competing interests. The contact author declare that they have not any competing interests.

Acknowledgements. Benjamin Kitambo has been supported by a doctoral grant from the French Space Agency (CNES), Agence Française du Développement (AFD), and Institut de Recherche pour le Développement (IRD). This research has been supported by the CNES TOSCA project "DYnamique hydrologique du BAssin du CoNGO (DYBANGO)" (2020–2023). We thank Dr Catherine Prigent from Sorbonne Université, Observatoire de Paris, Université PSL Paris, France for sharing the GIEMS-2 database.

Financial support. This research has been supported by the Centre National d'Etudes Spatiales (project TOSCA DYBANGO).

References

Albert, J.S.; Destouni, G.; Duke-Sylvester, S.M.; Magurran, A.E.; Oberdorff, T.; Reis, R.E.; Winemiller, K.O.; Ripple, W.J. Scientists' warning to humanity on the freshwater biodiversity crisis. Ambio, 50, 85–94, https://doi.org/10.1007/s13280-020-01318-8, 2021

Alsdorf, D.E.; Lettenmaier, D.P. Tracking fresh water from space. Science, 301, 1492–1494, DOI: 10.1126/science.1089802, 2003.

Alsdorf, D.E.; Rodríguez, E.; Lettenmaier, D.P. Measuring surface water from space. Rev. Geophys., 45, RG2002, https://doi.org/10.1029/2006RG000197, 2007.

Becker, M., Papa, F., Frappart, F., Alsdorf, D., Calmant, S., da Silva, J. S., Prigent, C., and Seyler, F.: Satellite-based estimates of surface water dynamics in the Congo River Basin, Int. J. Appl. Earth Obs. Ge oinf., 66, 196–209, https://doi.org/10.1016/j.jag.2017.11.015, 2018.

Beck, H. E., Pan, M., Roy, T., Weedon, G. P., Pappenberger, F., Dijk, A. I. J. M. Van, Huffman, G. J., Adler, R. F., and Wood, E. F. Daily evaluation of 26 precipitation datasets using Stage-IV gauge-radar data for the CONUS. *Hydrol. Earth Syst. Sci.*, *23*, 207–224. https://doi.org/https://doi.org/10.5194/hess-23-207-2019, 2019.

Beck, H. E., Vergopolan, N., Pan, M., Levizzani, V., Dijk, A. I. J. M. Van, Weedon, G. P., Brocca, L., Pappenberger, F., Huffman, G. J., and Wood, E. F. Global-scale evaluation of 22 precipitation datasets using gauge observations and hydrological modeling. *Hydrol. Earth Syst. Sci.*, *21*, 6201–6217. https://doi.org/https://doi.org/10.5194/hess-21-6201-2017, 2017.

Beck, H. E., Wood, E. F., Pan, M., Fisher, C. K., Miralles, D. G., Dijk, A. I. J. M. van, McVicar, T. R., and Adler, R. F. MSWEP V2 Global 3-Hourly 0.1° Precipitation: Methodology and Quantitative Assessment. *Bull.*

Am. Meteorol. Soc., *100*(March), 473–500. https://doi.org/https://doi.org/10.1175/BAMS-D-17-0138.1, 2019.

Becker, M., Papa, F., Frappart, F., Alsdorf, D., Calmant, S., da Silva, J. S., Prigent, C., and Seyler, F. Satellite-based estimates of surface water dynamics in the Congo River Basin. *Int. J. Appl. Earth Obs. Geoinf.*, *66* (8), 196–209. https://doi.org/10.1016/j.jag.2017.11.015, 2018.

Biancamaria, S., Lettenmaier, D. P., Pavelsky, T. M. The SWOT Mission and Its Capabilities for Land Hydrology. Surveys in Geophysics, 37(2), 307–337. https://doi.org/10.1007/s10712-015-9346-y, 2016.

Biddulph, G. E., Bocko, Y. E., Bola, P., Crezee, B., Dargie, G. C., Emba, O., Georgiou, S., Girkin, N., Hawthorne, D., Jonay Jovani-Sancho, A., Joseph Kanyama, T., Mampouya, W. E., Mbemba, M., Sciumbata, M., and Tyrrell, G. Current knowledge on the Cuvette Centrale peatland complex and future research directions. *Bois Forets des Trop.*, *350*, 3–14. https://doi.org/10.19182/bft2021.350.a36288, 2021.

Boberg, J. Freshwater Availability. In Liquid Assets: How Demographic Changes and Water Management Policies Affect Freshwater Resources; RAND Corporation: Santa Monica, CA, USA; Arlington, VA, USA; Pittsburgh, PA, USA, pp. 15–28. Available online: http://www.jstor.org/stable/10.7249/mg358cf.9 (last access on ~~2~~17 May~~September~~ 202~~32~~), 2005.

Bogning, S., Frappart, F., Blarel, F., Niño, F., Mahé, G., Bricquet, J. P., Seyler, F., Onguéné, R., Etamé, J., Paiz, M. C., and Braun, J. J.: Monitoring water levels and discharges using radar altimetry in an ungauged river basin: The case of the Ogooué, Remote Sens., 10, 350, https://doi.org/10.3390/rs10020350, 2018.

Bricquet, J.-P.: Les écoulements du Congo à Brazzaville et la spatialisation des apports, in: Grands bassins fluviaux périatlantiques: Congo, Niger, Amazone, Paris, ORSTOM, edited by: Boulègue, J. and Olivry, J.-C., Colloques et Séminaires, Grands Bassins Fluviaux Péri-Atlantiques: Congo, Niger, Amazone, Paris, France, 1993/11/22-24, 27–38, ISBN 2-7099-1245-7, ISSN 0767-2896, 1995.

Bullock, A., Acreman, M. The role of wetlands in the hydrological cycle. Hydrol. Earth Syst. Sci., 7, 358–389. doi:10.5194/hess-7-358-2003, 2003.

Cazenave, A., Champollion, N., Benveniste, J., and Chen, J. Remote Sensing and Water Resources Management. In A. Cazenave, N. Champollion, J. Benveniste, and J. Chen (Eds.), *J. Am. Water Resour. Assoc.*,10 (4). Springer. https://doi.org/10.1111/j.1752-1688.1974.tb05660.x, 2016.

Chahine, M.T. The hydrological cycle and its influence on climate. Nature, 359, 373–380, https://doi.org/10.1038/359373a0, 1992

Cooley, S.W.; Ryan, J.C.; Smith, L.C. Human alteration of global surface water storage variability. Nature, 591, 78–81, https://doi.org/10.1038/s41586-021-03262-3, 2021.

Crétaux, J. F., Arsen, A., Calmant, S., Kouraev, A., Vuglinski, V., Bergé-Nguyen, M., Gennero, M. C., Nino, F., Abarca Del Rio, R., Cazenave, A., and Maisongrande, P. SOLS: A lake database to monitor in the Near Real Time water level and storage variations from remote sensing data. *Adv. Sp. Res.*, *47*(9), 1497–1507. https://doi.org/10.1016/j.asr.2011.01.004, 2011.

Cretaux, J., Frappart, F., Papa, F., Calmant, S., Nielsen, K., and Benveniste, J.: Hydrological Applications of Satellite Altimetry Rivers, Lakes, Man-Made Reservoirs, Inundated Areas, in: Satellite Altimetry over Oceans and Land Surfaces, edited by: Stammer, D. C. and Cazenave, A., Taylor & Francis Group, New York, 459–504, ISBN 9781315151779, https://doi.org/10.1201/9781315151779, 2017.

Crezee, B., Dargie, G. C., Ewango, C. E. N., Mitchard, E. T. A., B, O. E., T, J. K., Bola, P., Ndjango, J. N., Girkin,

Code de champ modifié

N. T., Bocko, Y. E., Ifo, S. A., Hubau, W., Seidensticker, D., Batumike, R., Wotzka, H., Bean, H., Baker, T. R., Baird, A. J., Boom, A., … Lewis, S. L. Mapping peat thickness and carbon stocks of the central Congo Basin using field data. Nature Geoscience, 15, 639–644. https://doi.org/10.1038/s41561-022-00966-7, 2022.

Crowley, J. W., Mitrovica, J. X., Bailey, R. C., Tamisiea, M. E., Davis, J. L. Land water storage within the Congo Basin inferred from GRACE satellite gravity data. Geophysical Research Letters, 33(19). https://doi.org/10.1029/2006GL027070, 2006.

Da Silva, J., Calmant, S., Seyler, F., Corrêa, O., Filho, R., Cochonneau, G., and João, W.: Water levels in the Amazon basin derived from the ERS 2 and ENVISAT radar altimetry missions, Remote Sens. Environ., 114, 2160–2181, https://doi.org/10.1016/j.rse.2010.04.020, 2010.

Datok, P., Fabre, C., Sauvage, S., Moukandi N'kaya, G. D., Paris, A., Dos Santos, V., Guilhen, J., Manteaux S, Laraque, A., and Sanchez Perez, J. M. Investigating the role of the Cuvette Centrale wetlands in the hydrology, sediment and carbon fluxes of the Congo River Basin (CRB). *Earth Sp. Sci. Open Arch.*. https://doi.org/https://doi.org/10.1002/essoar.10505504.1, 2020.

Decharme, B., Alkama, R., Papa, F., Faroux, S., Douville, H., and Prigent, C.: Global off-line evaluation of the ISBA-TRIP flood model, Clim. Dynam., 38, 1389–1412, https://doi.org/10.1007/s00382-011-1054-9, 2011.

de Marsily, G.: Eaux continentales, C. R. Geosci., 337, 1–2, 2005. Decharme, B., Douville, H., Prigent, C., Papa, F., and Aires, F.: A new river flooding scheme for global climate applications: Off-line validation over South America, J. Geophys. Res., 113, D11110, doi:10.1029/2007JD009376, 2008.

Dubayah, R., Blair, J.B., Goetz, S., Fatoyinbo, L., Hansen, M., Healey, S., Hofton, M., Hurtt, G., Kellner, J., Luthcke, S. The global ecosystem dynamics investigation: high-resolution laser ranging of the Earth's forests and topography. Sci. Remote Sens. 1, 100002, https://doi.org/10.1016/j.srs.2020.100002, 2020a.

Fassoni-Andrade, A. C., Fleischmann, A. S., Papa, F., Paiva, R. C. D. d., Wongchuig, S., Melack, J. M., et al. Amazon hydrology from space: Scientific advances and future challenges. Reviews of Geophysics, 59, e2020RG000728. https://doi.org/10.1029/2020RG000728, 2021.

Frappart, F., Calmant, S., Cauhopé, M., Seyler, F., and Cazenave, A.: Preliminary results of ENVISAT RA-2-derived water levels validation over the Amazon basin, Remote Sens. Environ., 100, 252–264, https://doi.org/10.1016/j.rse.2005.10.027, 2006.

Frappart, F.; Papa, F.; Famiglietti, J.; Prigent, C.; Rossow, W.B.; Seyler, F. Interannual variations of river water storage from a multiple satellite approach: A case study for the Rio Negro River basin. J. Geophys. Res., 113, 113, https://doi.org/10.1029/2007JD009438, 2008.

Frappart, F.; Papa, F.; Güntner, A.; Werth, S.; Ramillien, G.; Prigent, C.; Rossow, W.B.; Bonnet, M.-P. Interannual variations of the terrestrial water storage in the Lower Ob' Basin from a multisatellite approach. Hydrol. Earth Syst. Sci., 14, 2443–2453, https://doi.org/10.5194/hess-14-2443-2010, 2010.

Frappart, F., Papa, F., Güntner, A., Werth, S., Santos da Silva, J., Tomasella, J., Seyler, F., Prigent, C., Rossow, W. B., Calmant, S., & Bonnet, M. P. Satellite-based estimates of groundwater storage variations in large drainage basins with extensive floodplains. Remote Sens. Environ., 115(6), 1588–1594. https://doi.org/10.1016/j.rse.2011.02.003, 2011.

Frappart, F.; Papa, F.; Da Silva, J.S.; Ramillien, G.; Prigent, C.; Seyler, F.; Calmant, S. Surface freshwater storage and dynamics in the Amazon basin during the 2005 exceptional drought. Environ. Res. Lett., 7, 7,

https://iopscience.iop.org/article/10.1088/1748-9326/7/4/044010, 2012.

Frappart, F.; Papa, F.; Malbéteau, Y.; Leon, J.G.; Ramillien, G.; Prigent, C.; Seoane, L.; Seyler, F.; Calmant, S. Surface freshwater storage variations in the Orinoco floodplains using multi-satellite observations. Remote Sens., 7, 89–110, https://doi.org/10.3390/rs70100089, 2015.

Frappart, F., Papa, F., Marieu, V., Malbeteau, Y., Jordy, F., Calmant, S., Durant, F., Bala, S. Preliminary assessment of SARAL/AltiKa observations over the Ganges-Brahmaputra and Irrawaddy Rivers. Marine Geodesy, 38(sup1), 568-580, DOI: 10.1080/01490419.2014.990591, 2015b.

Frappart, F., Legrésy, B., Nino, F., Blarel, F., Fuller, N., Fleury, S., Birol, F., Calmant, S. An ERS-2 altimetry reprocessing compatible with ENVISAT for long-term land and ice sheets studies. Remote Sens. Environ., 184, 558-581, https://doi.org/10.1016/j.rse.2016.07.037, 2016.

Frappart, F.; Biancamaria, S.; Normandin, C.; Blarel, F.; Bourrel, L.; Aumont, M.; Azemar, P.; Vu, P.-L.; Le Toan, T.; Lubac, B.; et al. Influence of recent climatic events on the surface water storage of the Tonle Sap Lake. Sci. Total. Environ., 636, 1520–1533, https://doi.org/10.1016/j.scitotenv.2018.04.326, 2018.

Frappart, F.; Papa, F.; Güntner, A.; Tomasella, J.; Pfeffer, J.; Ramillien, G.; Emilio, T.; Schietti, J.; Seoane, L.; da Silva Carvalho, J.; Medeiros Moreira, D., Bonnet, M.P., Seyler, F. The spatio-temporal variability of groundwater storage in the Amazon River Basin. Adv. Water Resour., 124, 41–52, https://doi.org/10.1016/j.advwatres.2018.12.005, 2019.

Frappart, F., Blarel, F., Fayad, I., Bergé-Nguyen, M., Crétaux, J. F., Shu, S., Schregenberger, J., Baghdadi, N. Evaluation of the performances of radar and lidar altimetry missions for water level retrievals in mountainous environment: The case of the Swiss lakes. Remote Sensing, 13(11), 2196, https://doi.org/10.3390/rs13112196, 2021b.

Good, S.P.; Noone, D.; Bowen, G. Hydrologic connectivity constrains partitioning of global terrestrial water fluxes. Science, 349, 175–177, DOI: 10.1126/science.aaa5931, 2015

Gasse, F., Ledee, V., Massauh, M., and Fontes, J. Water-level fluctuations of Lake Tanganyika in phase with oceanic changes during the last glaciation and deglaciation. *Nature*, *342*, 57–59. https://doi.org/https://doi.org/10.1038/342057a0, 1989.

Guth, P. L., Van Niekerk, A., Grohmann, C. H., Muller, J. P., Hawker, L., Florinsky, I. V., Gesch, D., Reuter, H. I., Herrera-Cruz, V., Riazanoff, S., López-Vázquez, C., Carabajal, C. C., Albinet, C., Strobl, P. Digital elevation models: Terminology and definitions. Remote Sens., 13(18), 1–19. https://doi.org/10.3390/rs13183581, 2021.

Harrison, I. J., Brummett, R., and Stiassny, M. L. J. The Congo River Basin. In C. M. Finlayson, A. A. van Dam, K. Irvine, M. Everard, R. J. McInnes, B. A. Middleton, and N. C. Davidson (Eds.), *The Wetland Book* (1). Springer Science+Business Media Dordrecht. https://doi.org/10.1007/978-94-007-6173-5, 2016.

Hastie, A., Lauerwald, R., Ciais, P., Papa, F., Regnier, P. Historical and future contributions of inland waters to the Congo Basin carbon balance. Earth System Dynamics, 12(1), 37–62. https://doi.org/10.5194/esd-12-37-2021, 2021.

Hawker, L., Neal, J., and Bates, P. Accuracy assessment of the TanDEM-X 90 Digital Elevation Model for selected floodplain sites. *Remote Sens. Environ.*, *232*(11). https://doi.org/10.1016/j.rse.2019.111319, 2019.

Hawker, L., Uhe, P., Paulo, L., Sosa, J., Savage, J., Sampson, C., Neal, J. A 30 m global map of elevation with forests and buildings removed. Environ. Res. Lett., 17(2). https://doi.org/10.1088/1748-9326/ac4d4f, 2022.

Code de champ modifié

Hua, W., Zhou, L., Chen, H., Nicholson, S. E., Raghavendra, A., and Jiang, Y. Possible causes of the Central Equatorial African long-term drought Possible causes of the Central Equatorial African long-term drought. *Environ. Res. Lett.*, *11*. http://dx.doi.org/10.1088/1748-9326/11/12/124002, 2016.

Huffman, G.J., E.F. Stocker, D.T. Bolvin, E.J. Nelkin, Jackson Tan. GPM IMERG Final Precipitation L3 Half Hourly 0.1 degree x 0.1 degree V06, Greenbelt, MD, Goddard Earth Sciences Data and Information Services Center (GES DISC), Accessed: [~~2~~17 May~~September~~ 202~~3~~2], 10.5067/GPM/IMERG/3B-HH/06, 2019.

Inogwabini, B.-I.: The changing water cycle: Freshwater in the Congo, WIREs Water, 7, e1410, https://doi.org/10.1002/wat2.1410, 2020.

Jiang, L., Nielsen, K., Dinardo, S., Andersen, O. B., Bauer-Gottwein, P. Evaluation of Sentinel-3 SRAL SAR altimetry over Chinese rivers. *Remote Sensing of Environment*, *237*, 111546. https://doi.org/https://doi.org/10.1016/j.rse.2019.111546, 2020.

Kao, H., Kuo, C., Tseng, K., Shum, C. K., Tseng, T.-P., Jia, Y.- Y., Yang, T.-Y., Ali, T. A., Yi, Y., and Hussain, D.: Assessment of Cryosat-2 and SARAL/AltiKa altimetry for measuring inland water and coastal sea level variations: A case study on Tibetan Plateau Lake and Taiwan Coast, Mar. Geod., 42, 327–343, https://doi.org/10.1080/01490419.2019.1623352, 2019.

Kitambo, B., Papa, F., Paris, A., Tshimanga, R. M., Calmant, S., Fleischmann, A. S., Frappart, F., Becker, M., Tourian, M. J., Prigent, C., and Andriambeloson, J.: A combined use of in situ and satellite-derived observations to characterize surface hydrology and its variability in the Congo River basin, Hydrol. Earth Syst. Sci., 26, 1857–1882, https://doi.org/10.5194/hess-26-1857-2022, 2022a.

Kitambo, B., Papa, F., Paris, A., Tshimanga, R. M., Frappart, F., Calmant, S., Elmi, O., Fleischmann, A. S., Becker, M., Tourian, M. J., Jucá Oliveira, R. A., Wongchuig, S. A long-term monthly surface water storage dataset for the Congo basin from 1992 to 2015 [Data set]. Zenodo. https://doi.org/10.5281/zenodo.7299823, 2022b.

Kittel, C. M. M., Jiang, L., Tøttrup, C., and Bauer-Gottwein, P.: Sentinel-3 radar altimetry for river monitoring - A catchmentscale evaluation of satellite water surface elevation from Sentinel-3A and Sentinel-3B, Hydrol. Earth Syst. Sci., 25, 333–357, https://doi.org/10.5194/hess-25-333-2021, 2021.

Laraque, Alain, Bricquet, J. P., Pandi, A., and Olivry, J. C.: A review of material transport by the Congo River and its tributaries, Hydrol. Process., 23, 3216–3224, https://doi.org/10.1002/hyp.7395, 2009.

Laraque, A., Bellanger, M., Adele, G., Guebanda, S., Gulemvuga, G., Pandi, A., Paturel, J. E., Robert, A., Tathy, J. P., and Yambele, A.: Evolutions récentes des débits du Congo, de l'Oubangui et de la Sangha, Geo-Eco-Trop., 37, 93–100, http://www.geoecotrop.be/uploads/publications/pub_371_06.pdf (last access on ~~2~~17/0~~5~~9/202~~3~~2), 2013.

Laraque, A., N'kaya, G. D. M., Orange, D., Tshimanga, R., Tshitenge, J. M., Mahé, G., Nguimalet, C. R., Trigg, M. A., Yepez, S., and Gulemvuga, G.: Recent budget of hydroclimatology and hydrosedimentology of the congo river in central Africa. Water, 12(9). https://doi.org/10.3390/w12092613, 2020.

Lee, H., Beighley, R. E., Alsdorf, D., Chul, H., Shum, C. K., Duan, J., Guo, J., Yamazaki, D., and Andreadis, K.: Remote Sensing of Environment Characterization of terrestrial water dynamics in the Congo Basin using GRACE and satellite radar altimetry, Remote Sens. Environ., 115, 3530–3538, https://doi.org/10.1016/j.rse.2011.08.015, 2011.

a mis en forme : Français(France)

a mis en forme : Français(France)

a mis en forme : Français(France)

Code de champ modifié

Code de champ modifié

Mcphaden, M. J. El Ni no and La Ni na : Causes and Global Consequences. In Encyclopedia of Global Environmental Change (1), pp. 1–17, ISBN 0-471-97796-9, https://www.pmel.noaa.gov/gtmba/files/PDF/pubs/ElNinoLaNina.pdf (last access: ~~2~~17 May~~September~~ 2023~~2~~), 2002.

Mekonnen, M.M.; Hoekstra, A.Y. Sustainability: Four billion people facing severe water scarcity. Sci. Adv., 2, e1500323, DOI: 10.1126/sciadv.1500323, 2016.

Melack, J.M., Forsberg, B.R. Biogeochemistry of Amazon floodplain lakes and associated wetlands. In The Bio-Geochemistry of the Amazon Basin; McClain, M.E., Victoria, R.L., Richey, J.E., Eds.; Oxford University Press: New York, NY, USA, pp. 235–274, DOI: 10.1093/oso/9780195114317.001.0001, 2001.

Ndehedehe, C. E., Awange, J. L., Agutu, N. O., and Okwuashi, O. Changes in hydro-meteorological conditions over tropical West Africa (1980 – 2015) and links to global climate. *Glob. Planet. Change*, *162* (2), 321–341. https://doi.org/10.1016/j.gloplacha.2018.01.020, 2018.

Ndehedehe, C. E., Anyah, R. O., Alsdorf, D., Agutu, N. O., and Ferreira, V. G. Modelling the impacts of global multi-scale climatic drivers on hydro-climatic extremes (1901 – 2014) over the Congo basin. *Sci. Total Environ.*, *651*, 1569–1587. https://doi.org/10.1016/j.scitotenv.2018.09.203, 2019.

Ndehedehe, C. E., and Agutu, N. O. Historical Changes in Rainfall Patterns over the Congo Basin and Impacts on Runoff (1903 – 2010). In R. M. Tshimanga, G. D. M. N'kaya, & D. Alsdorf (Eds.), Congo Basin Hydrology, Climate, and Biogeochemistry A Foundation for the Future. American Geophysical Union and John Wiley and Sons, Inc. https://doi.org/10.1002/9781119657002.ch9, 2022.

Normandin, C.; Frappart, F.; Lubac, B.; Bélanger, S.; Marieu, V.; Blarel, F.; Robinet, A.; Guiastrennec-Faugas, L. Quantification of surface water volume changes in the Mackenzie Delta using satellite multi-mission data. Hydrol. Earth Syst. Sci., 22, 1543–1561, https://doi.org/10.5194/hess-22-1543-2018, 2018.

O'Connell, E. Towards Adaptation ofWater Resource Systems to Climatic and Socio-Economic Change. Water Resour. Manag., 31, 2965–2984, https://doi.org/10.1007/s11269-017-1734-2, 2017.

O'Loughlin, F. E., Paiva, R. C. D., Durand, M., Alsdorf, D. E., Bates, P. D. A multi-sensor approach towards a global vegetation corrected SRTM DEM product. Remote Sensing of Environment, 182, 49–59. https://doi.org/https://doi.org/10.1016/j.rse.2016.04.018, 2016.

Oki, T.; Kanae, S. Global Hydrological Cycles and WorldWater Resources. Science, 313, 1068–1072, DOI: 10.1126/science.1128845, 2006.

Prigent, Catherine, Papa, F., Aires, F., Rossow, W. B., and Matthews, E.: Global inundation dynamics inferred from multiple satellite observations, 1993–2000, J. Geophys. Res.-Atmos., 112, 1993–2000, https://doi.org/10.1029/2006JD007847, 2007.

Prigent, C., Jimenez, C., Bousquet, P. Satellite-derived global surface water extent and dynamics over the last 25 years (GIEMS-2). J. Geophys. Res. Atmos., 125, e2019JD030711. https://doi.org/10.1029/2019JD030711, 2020.

Papa, F, Gu, A., Frappart, F., Prigent, C., and Rossow, W. B.: Variations of surface water extent and water storage in large river basins: A comparison of different global data sources, Geophys. Res. Lett., 35, 1–5, https://doi.org/10.1029/2008GL033857, 2008.

Papa, F., Prigent, C., Aires, F., Jimenez, C., Rossow, W. B., and Matthews, E.: Interannual variability of surface water extent at the global scale, 1993–2004, J. Geophys. Res.-Atmos., 115, 1–17, https://doi.org/10.1029/2009JD012674, 2010.

Papa, F., Frappart, F., Güntner, A., Prigent, C., Aires, F., Getirana, A. C. V., and Maurer, R.: Surface freshwater storage and variability in the Amazon basin from multi-satellite observations, 1993–2007, J. Geophys. Res.-Atmos., 118, 11951–11965, https://doi.org/10.1002/2013JD020500, 2013.

Papa, F., Frappart, F., Malbeteau, Y., Shamsudduha, M., Vuruputur, V., Sekhar, M., Ramillien, G., Prigent, C., Aires, F., Pandey, R. K., Bala, S., and Calmant, S.: Satellitederived surface and sub-surface water storage in the Ganges- Brahmaputra River Basin, J. Hydrol. Reg. Stud., 4, 15–35, https://doi.org/10.1016/j.ejrh.2015.03.004, 2015.

Papa, F.; Frappart, F. SurfaceWater Storage in Rivers and Wetlands Derived from Satellite Observations: A Review of Current Advances and Future Opportunities for Hydrological Sciences. Remote Sens., 13, 4162. https:// doi.org/10.3390/rs13204162, 2021.

Paris, Adrien, De Paiva, R. D., Da Silva, J. S., Moreira, D. M., Calmant, S., Garambois, P.-A., Collischonn, W., Bonnet, M., and Seyler, F.: Stage-discharge rating curves based on satellite altimetry and modeled discharge in the Amazon basin, Water Resour. Res., 52, 3787–3814, https://doi.org/10.1002/2014WR016618, 2016.

Paris, A., Calmant, S., Gosset, M., Fleischmann, A. S., Conchy, T. S. X., Garambois, P.-A., Bricquet, J.-P., Papa, F., Tshimanga, R. M., Guzanga, G. G., Siqueira, V. A., Tondo, B.-L., Paiva, R., da Silva, J. S., and Laraque, A.: Monitoring Hydrological Variables from Remote Sensing and Modeling in the Congo River Basin, in: Congo Basin Hydrology, Climate, and Biogeochemistry edited by: Tshimanga, R. M., N'kaya, G. D. M., and Alsdorf, D., AGU, https://doi.org/10.1002/9781119657002.ch18, 2022.

Pervez, M. S., and Henebry, G. M. Spatial and seasonal responses of precipitation in the Ganges and Brahmaputra river basins to ENSO and Indian Ocean dipole modes : implications for flooding and drought. *Nat. Hazards Earth Syst. Sci.*, *15*, 147–162. https://doi.org/10.5194/nhess-15-147-2015, 2015.

Pham-duc, B., Papa, F., Prigent, C., Aires, F., Biancamaria, S., Frappart, F. Variations of Surface and Subsurface Water Storage in the Lower Mekong Basin (Vietnam and Cambodia) from Multisatellite Observations. Water, 11(1), 1–17. https://doi.org/10.3390/w11010075, 2019.

Pham-Duc, B.; Sylvestre, F.; Papa, F.; Frappart, F.; Bouchez, C.; Crétaux, J.-F. The Lake Chad hydrology under current climate change. Sci. Rep., 10, 5498, https://doi.org/10.1038/s41598-020-62417-w, 2020.

Potapov, P., Li, X., Hernandez-Serna, A., Tyukavina, A., Hansen, M.C., Kommareddy, A., Pickens, A., Turubanova, S., Tang, H., Silva, C.E., Armston, J., Dubayah, R., Blair, J. B., Hofton, M. Mapping and monitoring global forest canopy height through integration of GEDI and Landsat data, Remote Sens. Environ., 112165. https://doi.org/10.1016/j.rse.2020.112165, 2020.

Prigent, C., Jimenez, C., and Bousquet, P.: Satellite-Derived Global Surface Water Extent and Dynamics Over the Last 25 Years (GIEMS-2), J. Geophys. Res.-Atmos., 125, 1–21, https://doi.org/10.1029/2019JD030711, 2020.

Raymond, P.A.; Hartmann, J.; Lauerwald, R.; Sobek, S.; McDonald, C.; Hoover, M.; Butman, D.; Striegl, R.; Mayorga, E.; Humborg, C.; et al. Global carbon dioxide emissions from inland waters. Nature, 503, 355–359, https://doi.org/10.1038/nature12760, 2013.

Reis, V.; Hermoso, V.; Hamilton, S.K.; Ward, D.; Fluet-Chouinard, E.; Lehner, B.; Linke, S. A Global Assessment of Inland Wetland Conservation Status. Bioscience, 67, 523–533, https://doi.org/10.1093/biosci/bix045, 2017.

Richey, J.E.; Melack, J.M.; Aufdenkampe, A.; Ballester, V.M.; Hess, L.L. Outgassing from Amazonian rivers

and wetlands as a large tropical source of atmospheric CO2. Nature, 416, 617–620, https://doi.org/10.1038/416617a, 2002.

Richey, A. S., Thomas, B. F., Lo, M. H., Reager, J. T., Famiglietti, J. S., Voss, K., Swenson, S., Rodell, M. Quantifying renewable groundwater stress with GRACE. Water Resources Research, 51(7), 5217–5237. https://doi.org/10.1002/2015WR017349, 2015.

Rodell, M.; Beaudoing, H.K.; L'Ecuyer, T.S.; Olson,W.S.; Famiglietti, J.; Houser, P.R.; Adler, R.; Bosilovich, M.G.; Clayson, C.A.; Chambers, D.; et al. The Observed State of the Water Cycle in the Early Twenty-First Century. J. Clim., 28, 8289–8318, https://doi.org/10.1175/JCLI-D-14-00555.1, 2015.

Scanlon, B. R., Zhang, Z., Rateb, A., Sun, A., Wiese, D., Save, H., Beaudoing, H., Lo, M. H., Müller-Schmied, H., Döll, P., Beek, R. van, Swenson, S., Lawrence, D., Croteau, M., Reedy, R. C. Tracking Seasonal Fluctuations in Land Water Storage Using Global Models and GRACE Satellites. Geophysical Research Letters, 46(10), 5254–5264. https://doi.org/10.1029/2018GL081836, 2019.

Shelton, M.L. Hydroclimatology, Perspectives and applications, Cambridge University Press, New York, https://assets.cambridge.org/97805218/48886/frontmatter/9780521848886_frontmatter.pdf (last accessed: ~~2~~17/0~~59~~/202~~32~~), 2009.

Sridhar, V., Kang, H., Ali, S. A., Bola, G. B., Tshimanga, M. R., Lakshmi, V.: Bilan hydrique et sechéresse dans les conditions ctuelles et futures dans le bassin du fleuve Congo, in: Congo Basin Hydrology, Climate, and Biogeochemistry edited by: Tshimanga, R. M., N'kaya, G. D. M., and Alsdorf, D., AGU, https://doi.org/10.1002/9781119657002.ch18, 2022.

Stephens, G.L.; Slingo, J.M.; Rignot, E.; Reager, J.T.; Hakuba, M.Z.; Durack, P.J.; Worden, J.; Rocca, R. Earth's water reservoirs in a changing climate. Proc. R. Soc. A, 476, 20190458, https://doi.org/10.1098/rspa.2019.0458, 2020.

Steffen, W.; Richardson, K.; Rockström, J.; Cornell, S.E.; Fetzer, I.; Bennett, E.M.; Biggs, R.; De Carpenter, S.R.; Carpenter, S.R.; De Vries, W.; et al. Planetary boundaries: Guiding human development on a changing planet. Science, 347, 1259855, DOI: 10.1126/science.12598, 2015.

Tapley, B. D., Bettadpur, S., Watkins, M., & Reigber, C. The gravity recovery and climate experiment: Mission overview and early results. Geophysical research letters, 31(9), https://doi.org/10.1029/2004GL019920, 2004.

Tapley, B. D., Watkins, M. M., Flechtner, F., Reigber, C., Bettadpur, S., Rodell, M., ... & Velicogna, I. Contributions of GRACE to understanding climate change. Nature climate change, 9(5), 358-369, https://doi.org/10.1038/s41558-019-0456-2, 2019.

Tourian, M.J.; Reager, J.T.; Sneeuw, N. The Total Drainable Water Storage of the Amazon River Basin: A First Estimate Using GRACE. Water Resour. Res., 54, 3290–3312, https://doi.org/10.1029/2017WR021674, 2018.

Tourian, M. J., Elmi, O., Shafaghi, Y., Behnia, S., Saemian, P., Schlesinger, R., & Sneeuw, N. HydroSat: geometric quantities of the global water cycle from geodetic satellites. Earth System Science Data, 14(5), 2463-2486, doi: 10.5194/essd-2021-174, 2022.

~~Tourian, M. J., Papa, F., Elmi, O., Sneeuw, N., Kitambo, B., Tshimanga, R., Paris, A., Calmant S.: Current availability and distribution of Congo basin's freshwater resources, Research Square [preprint], https://doi.org/10.21203/rs.3.rs-1325377/v1, 21 September 2022.~~

Code de champ modifié

a mis en forme : Police :(Par défaut) Times New Roman, 10 pt, Couleur de police : Noir

a mis en forme : Justifié, Retrait : Gauche : 0 cm, Suspendu: 0,85 cm, Interligne: 1,5 ligne, Autoriser lignes veuves et orphelines, Bordure : Haut: (Pas de bordure), Bas: (Pas de bordure), Gauche: (Pas de bordure), Droite: (Pas de bordure), Entre : (Pas de bordure), Motif : Transparente

a mis en forme : Police :(Par défaut) Times New Roman, 10 pt, Non Gras, Couleur de police : Noir

a mis en forme : Police :(Par défaut) Times New Roman, 10 pt, Couleur de police : Noir

a mis en forme : Police :10 pt, Couleur de police : Noir, Anglais (États-Unis)

a mis en forme : Police :(Par défaut) Times New Roman, 10 pt, Couleur de police : Noir

a mis en forme : Police :(Par défaut) Times New Roman, 10 pt, Couleur de police : Noir, Motif : Transparente

a mis en forme : Police :(Par défaut) Times New Roman, 10 pt, Couleur de police : Noir

a mis en forme : Français (France)

Code de champ modifié

Tourian, M.J., Papa, F., Elmi, O., Sneeuw, N., Kitambo, B., Tshimanga, R., Paris, A., Calmant S.: Current availability and distribution of Congo Basin's freshwater resources. Commun Earth Environ 4, 174, https://doi.org/10.1038/s43247-023-00836-z, 2023.

Trenberth, K.E.; Smith, L.; Qian, T.; Dai, A.; Fasullo, J. Estimates of the global water budget and its annual cycle using observational and model data. J. Hydrometeorol., 8, 758–769, https://doi.org/10.1175/JHM600.1, 2007.

Trenberth, K.E.; Fasullo, J.; Mackaro, J. Atmospheric Moisture Transports from Ocean to Land and Global Energy Flows in Reanalyses. J. Clim., 24, 4907–4924, https://doi.org/10.1175/2011JCLI4171.1, 2011.

Tshimanga, R. M., N'kaya, G. D. M., & Alsdorf, D. Congo Basin Hydrology, Climate, and Biogeochemistry A Foundation for the Future (R. M. Tshimanga, G. D. M. N'kaya, & D. Alsdorf (eds.)). American Geophysical Union and John Wiley and Sons, Inc., 2022.

Ummenhofer, C. C., England, M. H., Mcintosh, P. C., Meyers, G. A., Pook, M. J., Risbey, J. S., and Gupta, A. Sen. What causes southeast Australia ' s worst droughts ? *Geophys. Res. Lett.*, *36*, 1–5. https://doi.org/10.1029/2008GL036801, 2009.

Verhegghen, A., Mayaux, P., De Wasseige, C., and Defourny, P.: Mapping Congo Basin vegetation types from 300m and 1 km multi-sensor time series for carbon stocks and forest areas estimation, Biogeosciences, 9, 5061–5079, https://doi.org/10.5194/bg-9-5061-2012, 2012.

Vörösmarty, C.J.; McIntyre, P.B.; Gessner, M.O.; Dudgeon, D.; Prusevich, A.; Green, P.; Glidden, S.; Bunn, S.E.; Sullivan, C.A.; Liermann, C.R.; et al. Global threats to human water security and river biodiversity. Nature, 467, 555–561, https://doi.org/10.1038/nature09440, 2010.

Ward, N.D.; Bianchi, T.; Medeiros, P.M.; Seidel, M.; Richey, J.E.; Keil, R.G.; Sawakuchi, H.O. Where Carbon Goes WhenWater Flows: Carbon Cycling across the Aquatic Continuum. Front. Mar. Sci., 4, https://doi.org/10.3389/fmars.2017.00007, 2017.

Watkins, M. M., D. N. Wiese, D.-N. Yuan, C. Boening, and F. W. Landerer. Improved methods for observing Earth's time variable mass distribution with GRACE using spherical cap mascons, J. Geophys. Res. Solid Earth, 120, doi:10.1002/2014JB011547, 2015.

White, L. J. T., Masudi, E. B., Ndongo, J. D., Matondo, R., Soudan-Nonault, A., Ngomanda, A., Averti, I. S., Ewango, C. E. N., Sonké, B., and Lewis, S. L.: Congo Basin rainforest - invest US$150 million in science. Nature, 598(7881), 411–414. https://doi.org/10.1038/d41586-021-02818-7, 2021.

Wiese, D. N., F. W. Landerer, and M. M. Watkins. Quantifying and reducing leakage errors in the JPL RL05M GRACE mascon solution, Water Resour. Res., 52, 7490–7502, doi:10.1002/2016WR019344, 2016.

Wiese, D.-N. Yuan, C. Boening, F. W. Landerer, M. M. Watkins. JPL GRACE Mascon Ocean, Ice, and Hydrology Equivalent Water Height Release 06 Coastal Resolution Improvement (CRI) Filtered Version 1.0. Ver. 1.0. PO.DAAC, CA, USA. Dataset accessed [2023-05-17] at http://dx.doi.org/10.5067/TEMSC-3MJC6, 2018.

Wohl, E. An Integrative Conceptualization of Floodplain Storage. Rev. Geophys., 59, e2020RG000724, https://doi.org/10.1029/2020RG000724, 2021.

Yamazaki D., Ikeshima, D., Tawatari, R., Yamaguchi, T., O'Loughlin, F., Neal, J.C., Sampson, C.C., Kanae, S., Bates, P.D. A high accuracy map of global terrain elevations, Geophys. Res. Lett., 44, pp.5844-5853, doi: 10.1002/2017GL072874, 2017.

a mis en forme : Police :(Par défaut) Times New Roman, Anglais (États-Unis)

a mis en forme : Anglais (États-Unis)

a mis en forme : Police :(Par défaut) Times New Roman, Anglais (États-Unis)

a mis en forme : Justifié, Retrait : Gauche : 0 cm, Suspendu: 0,85 cm, Interligne: 1,5 ligne, Autoriser lignes veuves et orphelines, Espacement automatique entre les caractères asiatiques et latins, Espacement automatique entre les caractères asiatiques et les chiffres, Bordure : Haut: (Pas de bordure), Bas: (Pas de bordure), Gauche: (Pas de bordure), Droite: (Pas de bordure), Entre : (Pas de bordure)

a mis en forme : Police :(Par défaut) Times New Roman, Anglais (États-Unis)

a mis en forme : Lien hypertexte, Police :(Par défaut) Times New Roman, Couleur de police : Automatique, Anglais (États-Unis)

a mis en forme : Police :(Par défaut) Times New Roman, Couleur de police : Noir, Anglais (États-Unis)

Code de champ modifié

a mis en forme : Police :(Par défaut) Times New Roman, 10 pt, Couleur de police : Noir, Motif : Transparente

a mis en forme : Police :10 pt, Couleur de police : Noir

a mis en forme : Police :(Par défaut) Times New Roman, 10 pt, Couleur de police : Noir, Motif : Transparente

a mis en forme : Police :(Par défaut) Times New Roman, 10 pt, Couleur de police : Noir, Motif : Transparente

a mis en forme : Police :(Par défaut) Times New Roman, 10 pt, Couleur de police : Noir, Motif : Transparente

a mis en forme : Police :(Par défaut) Times New Roman, 10 pt, Couleur de police : Noir, Motif : Transparente

Yuan T, Lee H, Jung CH, Aierken A, Beighley E, Alsdorf DE, Tshimanga RM, Kim D. Absolute water storages in the Congo River floodplains from integration of InSAR and satellite radar altimetry. Remote Sens Environ 201:57–72. https:// doi. org/ 10. 1016/j. rse. 2017. 09. 003, 2017.

Zakharova, E., Nielsen, K., Kamenev, G., and Kouraev, A.: River discharge estimation from radar altimetry: Assessment of satellite performance, river scales and methods, J. Hydrol., 583, 124561, https://doi.org/10.1016/j.jhydrol.2020.124561, 2020.

Zhou, T.; Nijssen, B.; Gao, H.; Lettenmaier, D.P. The Contribution of Reservoirs to Global Land Surface Water Storage Variations. J. Hydrometeorol., 17, 309–325, https://doi.org/10.1175/JHM-D-15-0002.1, 2016.

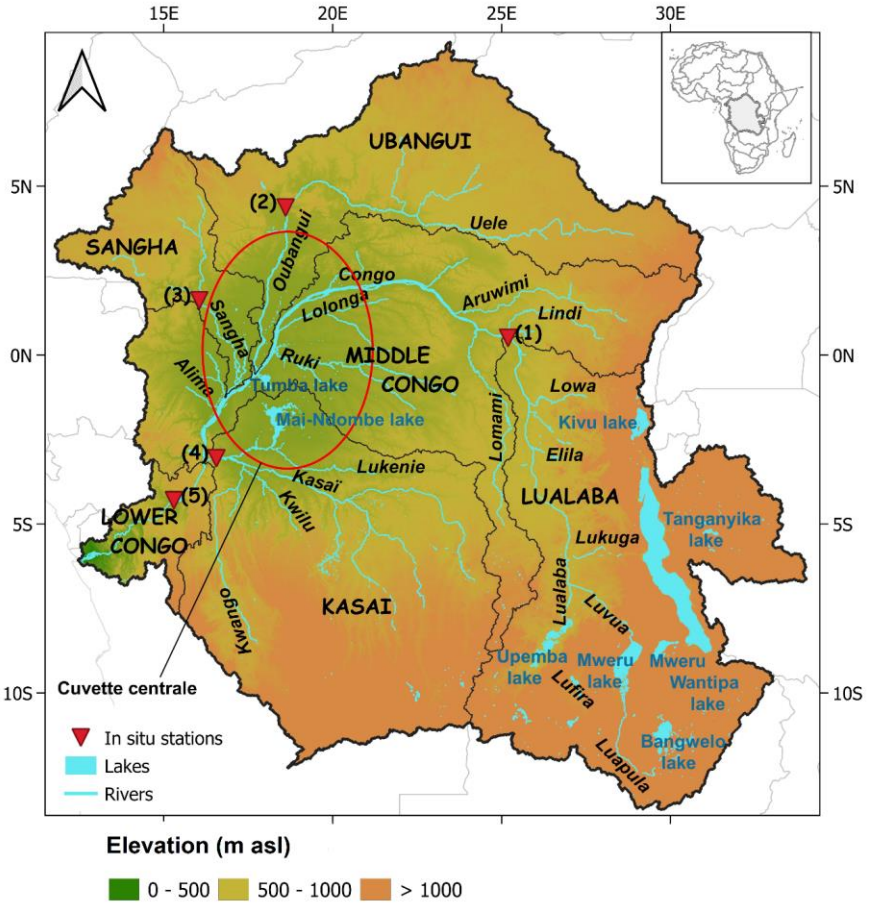

Figure 1: The Congo River basin (CRB) and its main subbasins (thin dark line), along with the major rivers and lakes (light blue color). The green portion in the central part circled by red line corresponds to the Cuvette Centrale. The background topography is derived from the Multi-Error-Removed Improved Terrain (MERIT) digital elevation model (DEM). The red triangles display the available in situ gauging stations, with their characteristics reported in Table 2.

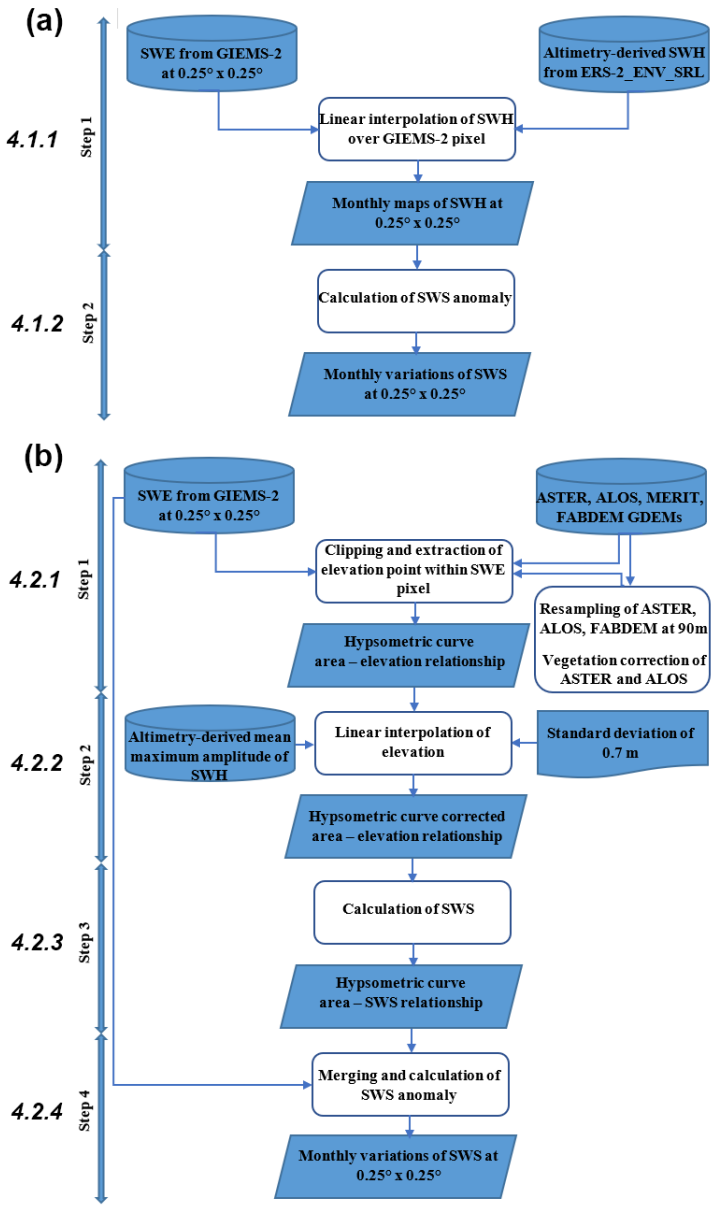

Figure 2: Schematic representation of (a) the multi-satellite and (b) hypsometric curve approaches algorithms. The numbers on the left refer to the sections where the different steps are described.

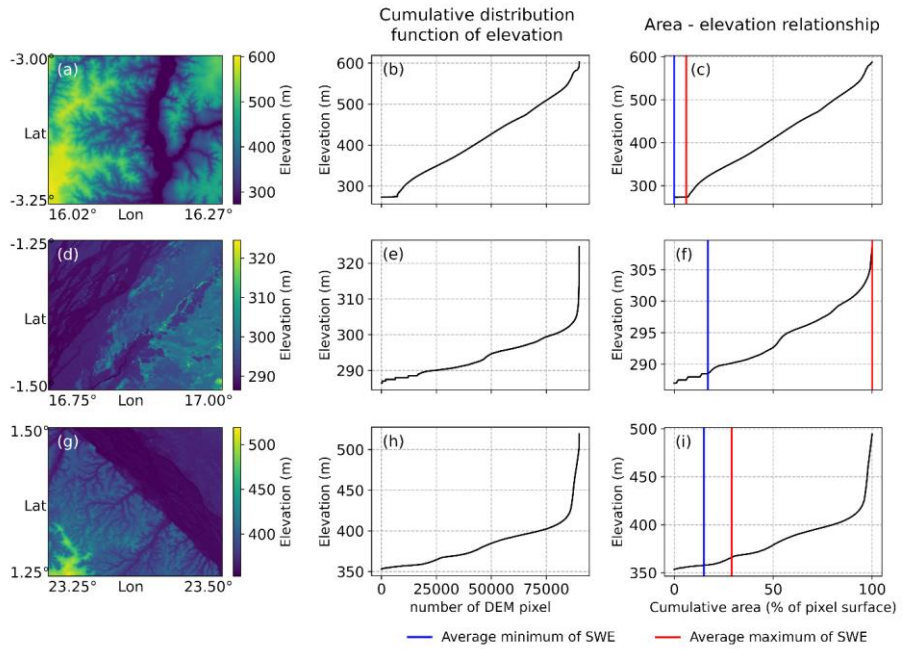

Figure 3: Hypsometric curve from FABDEM over the CRB. Left column: Map of FABDEM elevations within a 773 km^2 pixel of GIEMS-2. Middle column: The hypsometric curve from FABDEM, i.e., the distribution of elevation values in each 773 km^2 pixel sorted in ascending order. Right column: the hypsometric curve from FABDEM providing the relationship between the elevation and the inundated area of 773 km^2 pixel (as a percentage). The blue (red) line is the average minimum (maximum) coverage of SWE observed by GIEMS-2 over 1992-2015.

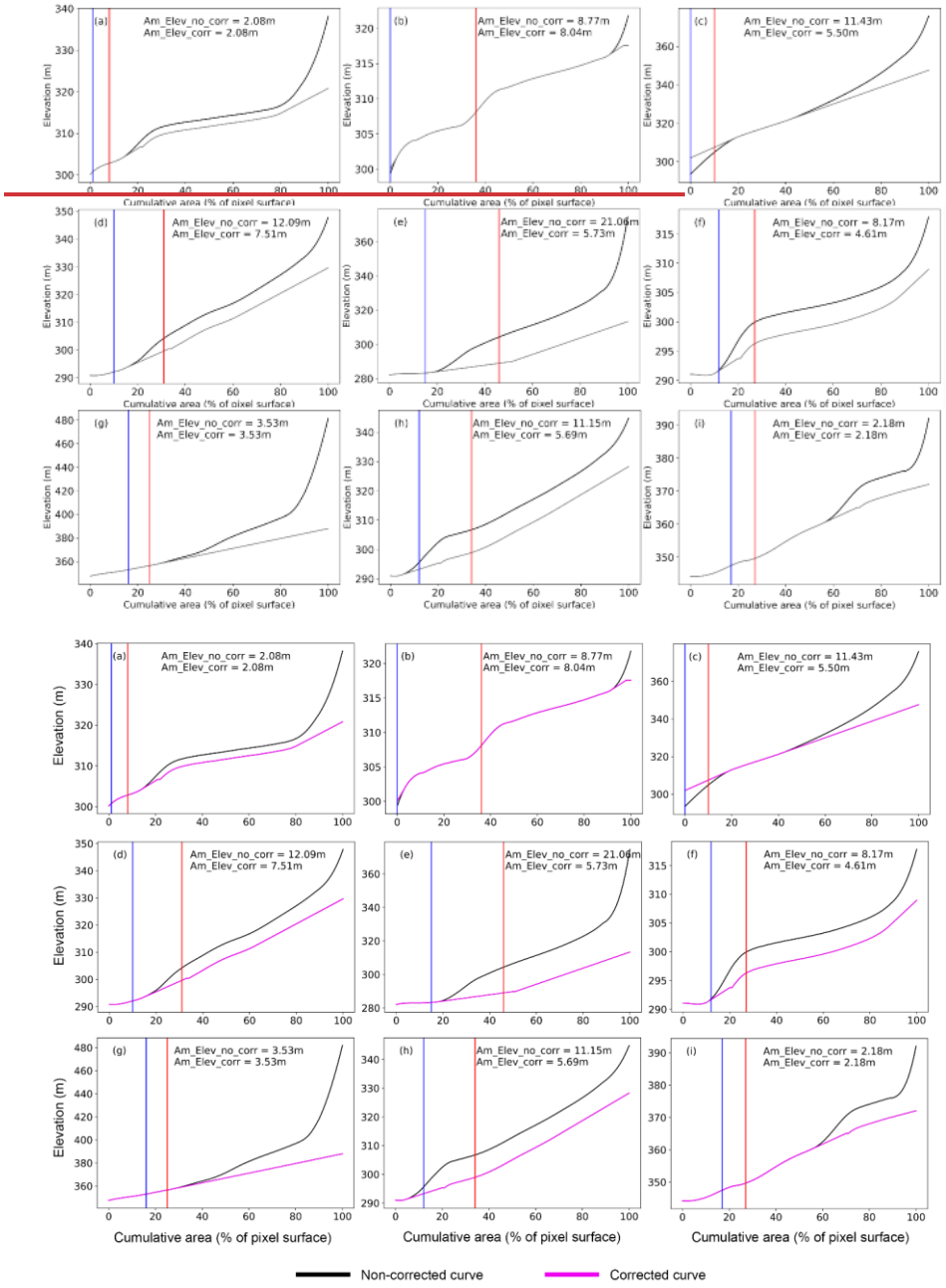

Figure 4: Correction of hypsometric curve from FABDEM by calculating the STD (m) of elevation over 5% flood coverage windows (see details of the procedure in section 4.2.2 ~~step 2~~). Black and magenta~~grey~~ curves stand respectively

1140 **for non-corrected and corrected hypsometric curve. Am_Elev_no_corr (from non-corrected curve) and Am_Elev_corr (from corrected curve) are the elevation amplitude derived from the average minimum (blue line) and maximum (red line) coverage of surface water extent observed by GIEMS-2 over 1992-2015. (a) to (i) show different pixels of GIEMS-2 in which the hypsometric curve is derived.**

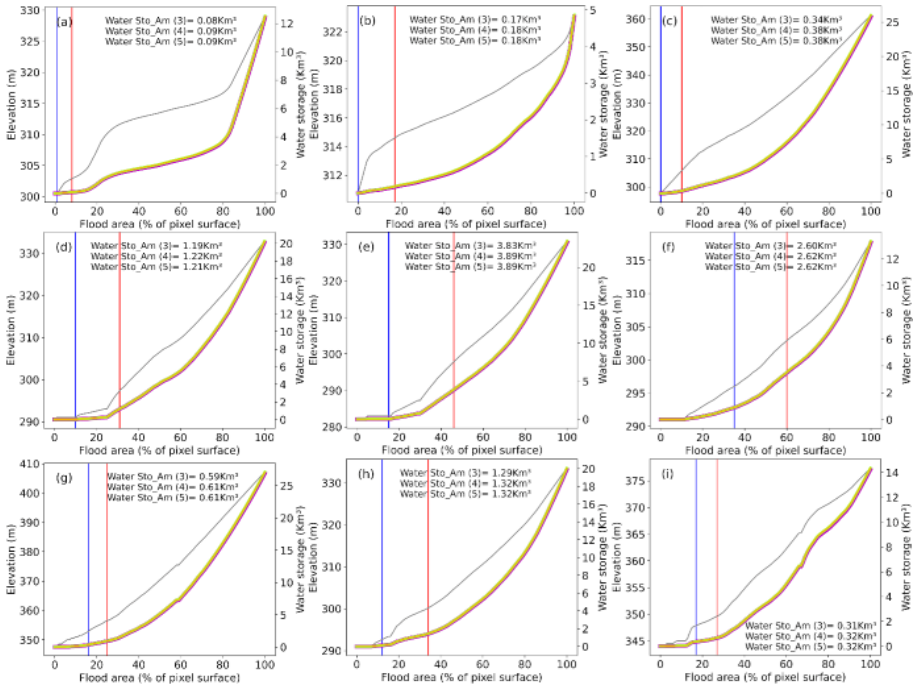

1145 **Figure 5: For the same GIEMS-2 pixel as in Fig. 3, the Surface Water Storage profile, i.e., the relationship between SWS within each GIEMS-2 pixel and the fractional inundated area of 773 km^2 in percentage (abscissa – right ordinate) obtained from the area-elevation relationship (abscissa – left ordinate). Magenta, green, orange colors are respectively the curve of SWS from the formulas (3), (4), and (5). The grey curve stands for the corrected FABDEM hypsometric**
1150 **curve. The blue (red) line is the average minimum (maximum) coverage of surface water extent observed by GIEMS-2 over 1992-2015. (a) to (i) represent different pixels of GIEMS-2 in which the hypsometric curve is derived.**

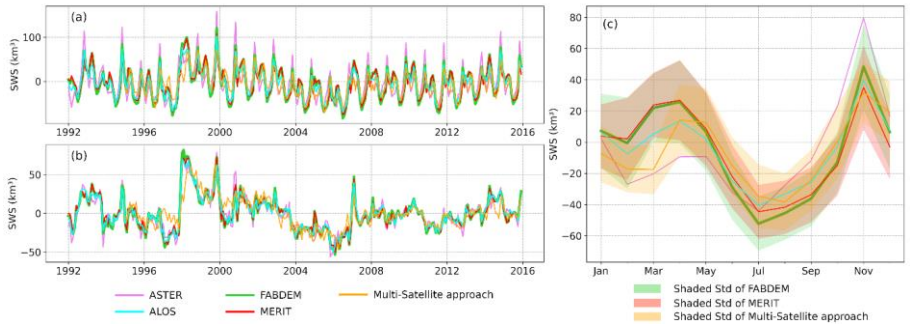

Figure 6: Long-term monthly time series of Congo River Basin's Surface Water Storage (a) and its deseasonalized anomaly (b) obtained from the hypsometric curve approach for 1992-2015 (violet for ASTER, aqua for ALOS, limegreen for FABDEM, red for MERIT) and from the multi-satellite approach for 1995-2015 (orange) (c) Annual cycles for each SWS estimate, with the shaded areas illustrating the standard deviations around their long-term mean.

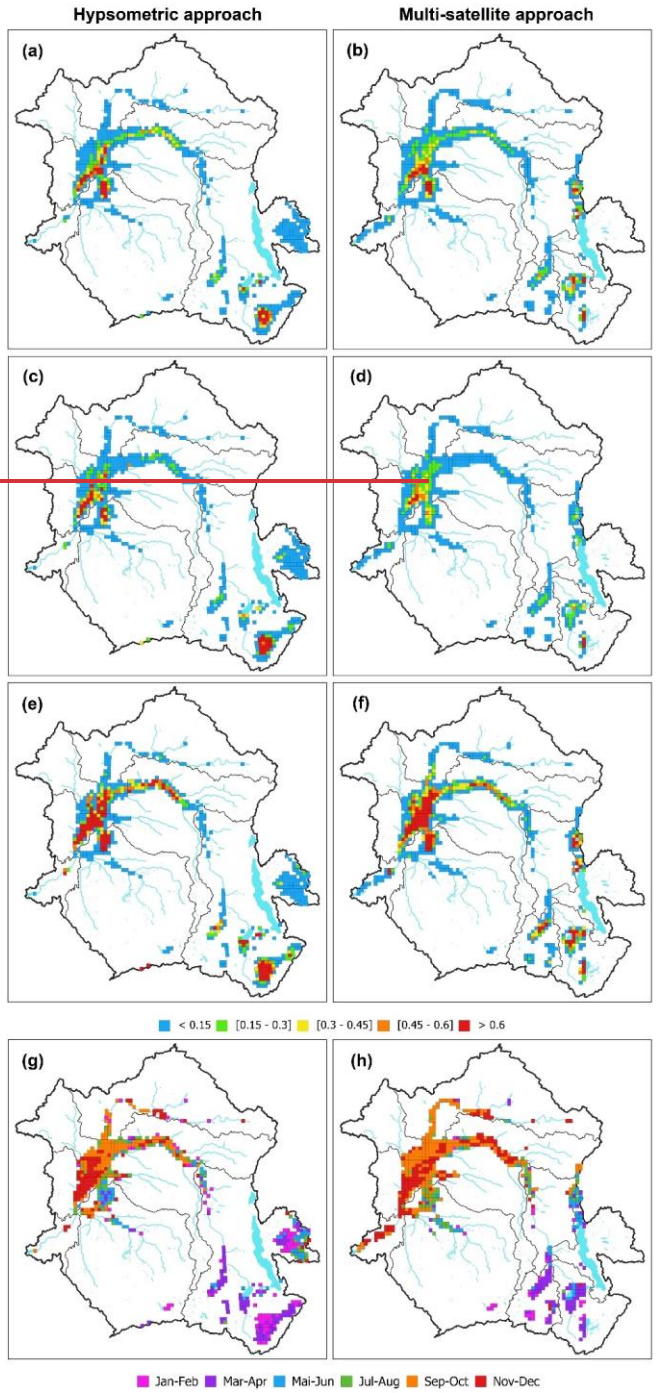
Hypsometric approach
Multi-satellite approach
(a)
(b)
(c)
(d)
(e)
(f)
< 0.15
[0.15 - 0.3]
[0.3 - 0.45]
[0.45 - 0.6]
> 0.6
(g)
(h)
Jan-Feb
Mar-Apr
Mai-Jun
Jul-Aug
Sep-Oct
Nov-Dec

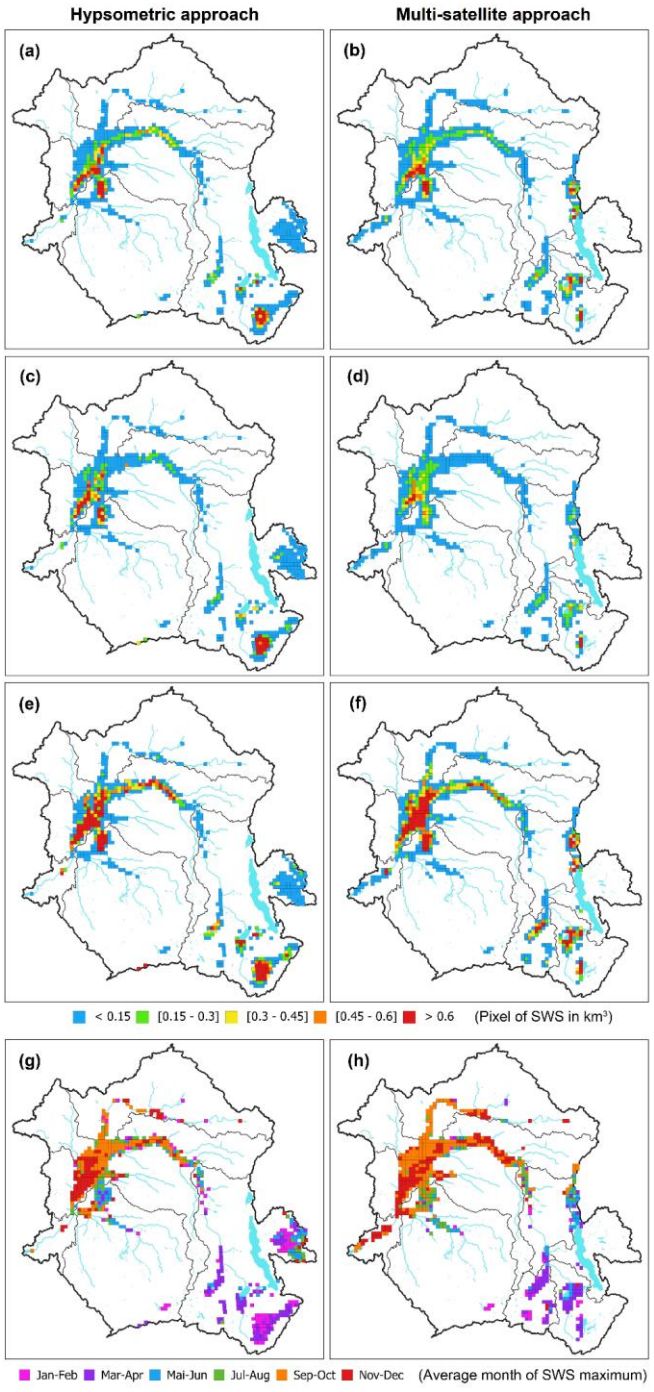
Hypsometric approach
Multi-satellite approach
(a)
(b)
(c)
(d)
(e)
(f)
< 0.15
[0.15 - 0.3]
[0.3 - 0.45]
[0.45 - 0.6]
> 0.6
(Pixel of SWS in km³)
(g)
(h)
Jan-Feb
Mar-Apr
Mai-Jun
Jul-Aug
Sep-Oct
Nov-Dec
(Average month of SWS maximum)

Figure 7: Spatial characterization of the CRB's SWS variations from the FABDEM hypsometric curve approach (over 1992– 2015, left column) and from the multi-satellite approach (over 1995-2015, right column). (a, b): SWS mean annual amplitude in km³; (c, d) Standard deviation (STD) in km³, (e, f) mean annual maximum in km³ and (g, h) average month of the maximum (in month).

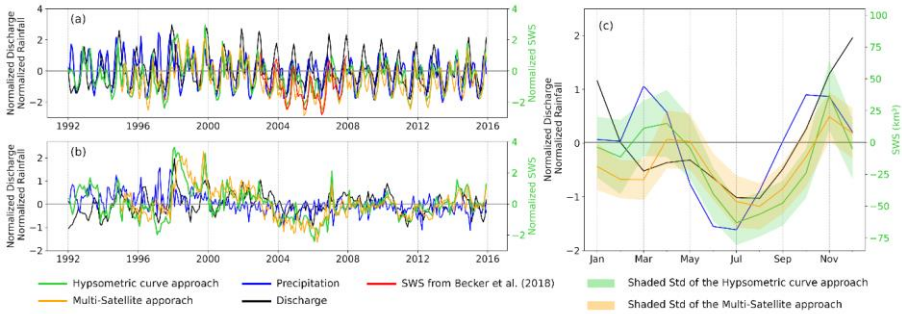

Figure 8: Comparison between the monthly aggregated normalized surface water storage anomaly, normalized precipitation anomaly over the basin and normalized discharge anomaly variations (at the outlet of CRB, Brazzaville/Kinshasa station) (for comparison purposes, SWS, precipitation and discharge were normalized by dividing their time series of anomalies by the standard deviation of the raw series). (a) For the entire Congo basin, the green and orange line represent respectively the SWS anomaly variations from hypsometric curve (over 1992-2015, from FABDEM) and multi-satellite (over 1995-2015) approaches, the red line shows SWS anomaly estimated by Becker et al. (2018) over 2003-2007, the black line is the discharge, the blue line is the normalized precipitation anomaly. (b) Deseasonalized normalized anomaly for SWS (green and orange), precipitation (blue), and discharge (black). (c) Normalized mean annual cycle for the three variables (except for the SWS), with the shaded areas depicting the standard deviations around the SWS anomaly.

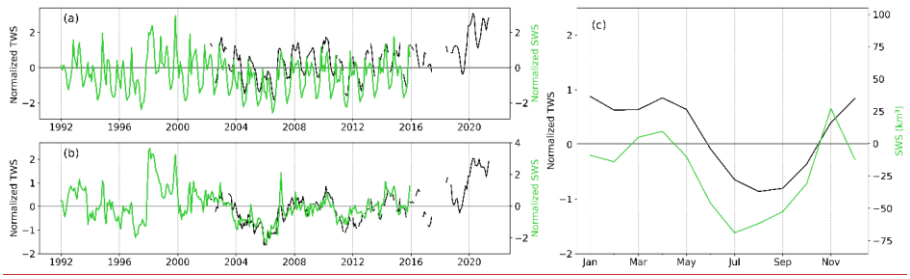

Figure 9. Comparison between the monthly aggregated normalized surface water storage anomaly and the normalized Terrestrial Water Storage Anomaly over the basin (for comparison purposes, SWS and TWSA were normalized by dividing their time series of anomalies by the standard deviation of the raw series). (a) For the entire Congo basin, the green and black line represent respectively the SWS anomaly variations from hypsometric curve approach (over 1992-2015, from FABDEM) and TWSA. (b) Deseasonalized normalized anomaly for SWS (green) and TWSA (black). (c) Normalized mean annual cycle for TWSA (black) (except for SWS, in green) calculated over the same period of data availability of the two variables, SWS and TWSA.

a mis en forme : Police :9 pt, Gras, Non Italique, Couleur de police : Noir

a mis en forme : Justifié, Espace Après : 0 pt, Interligne: 1,5 ligne, Ne pas ajuster l'espace entre le texte latin et asiatique, Ne pas ajuster l'espace entre le texte et les nombres asiatiques, Bordure : Haut: (Pas de bordure), Bas: (Pas de bordure), Gauche: (Pas de bordure), Droite: (Pas de bordure), Entre : (Pas de bordure)

a mis en forme : Police :9 pt, Gras, Non Italique, Couleur de police : Noir

a mis en forme : Police :9 pt, Gras

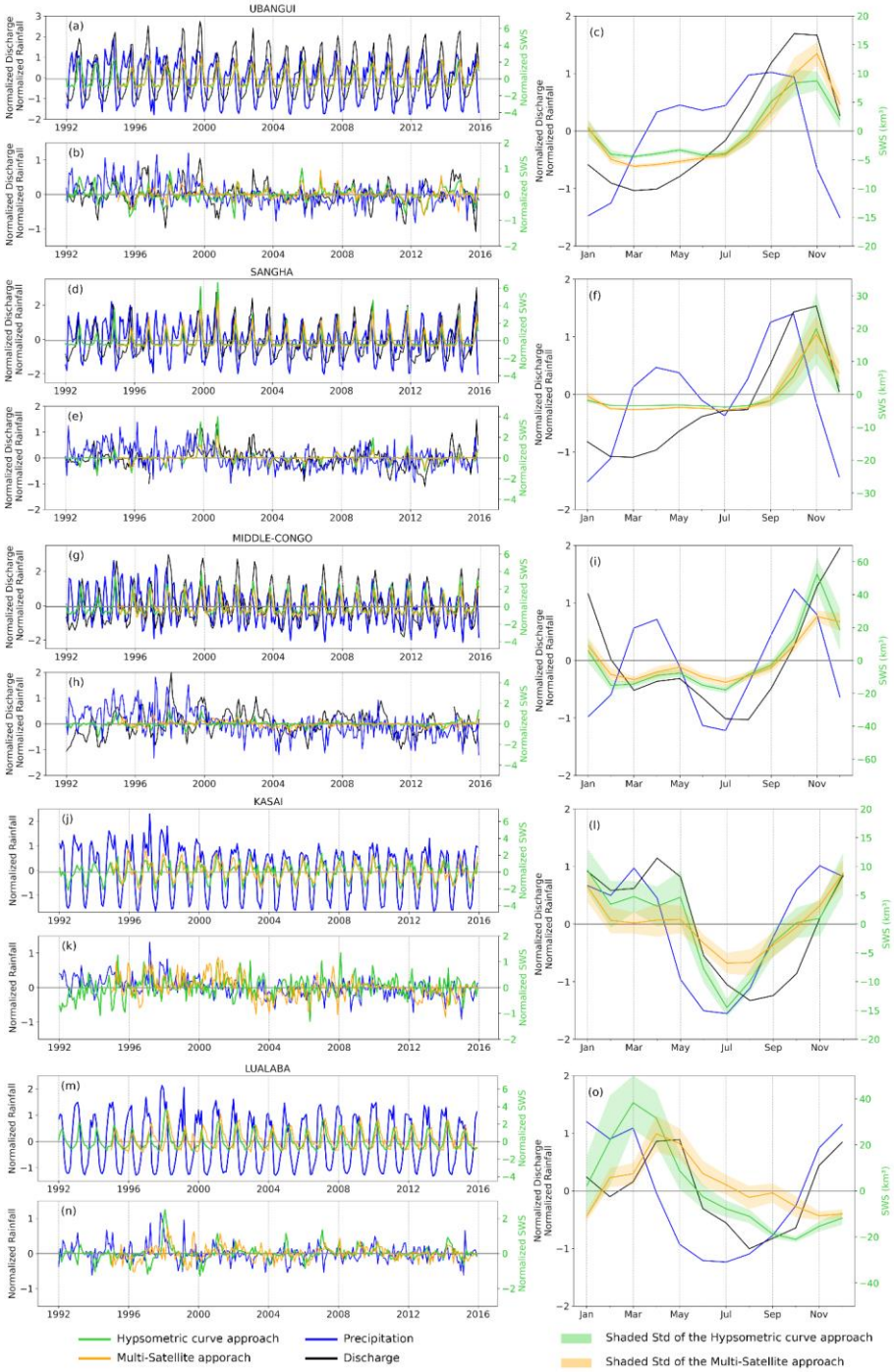
UBANGUI
SANGHA
MIDDLE-CONGO
KASAI
LUALABA
(a)
(b)
(c)
(d)
(e)
(f)
(g)
(h)
(i)
(j)
(k)
(l)
(m)
(n)
(o)
Normalized Discharge
Normalized Rainfall
Normalized SWS
SWS (km²)
Jan
Mar
May
Jul
Sep
Nov
Hypsometric curve approach
Multi-Satellite apporach
Precipitation
Discharge
Shaded Std of the Hypsometric curve approach
Shaded Std of the Multi-Satellite approach

Figure 109: Same to Fig. 8 but the discharge is considered at the outlets of each sub-basin, and the precipitation is the estimated mean over each sub-basin, both are compared to the normalized SWS anomaly variations. (a) For each sub-basin, the green and orange line represents respectively the SWS anomaly variations from hypsometric curve (over 1992-2015, from FABDEM) and multi-satellite (over 1995-2015) approaches, the red line shows SWS anomaly from Becker et al. (2018) over 2003-2007, the black line is the normalized discharge anomaly, the blue line is the normalized precipitation anomaly. (b) Deseasonalized normalized anomaly for SWS (green and orange), precipitation (blue), and discharge (black). (c) Normalized mean annual cycle for the three variables (except for the SWS), with the shaded areas depicting the standard deviations around the SWS anomaly.

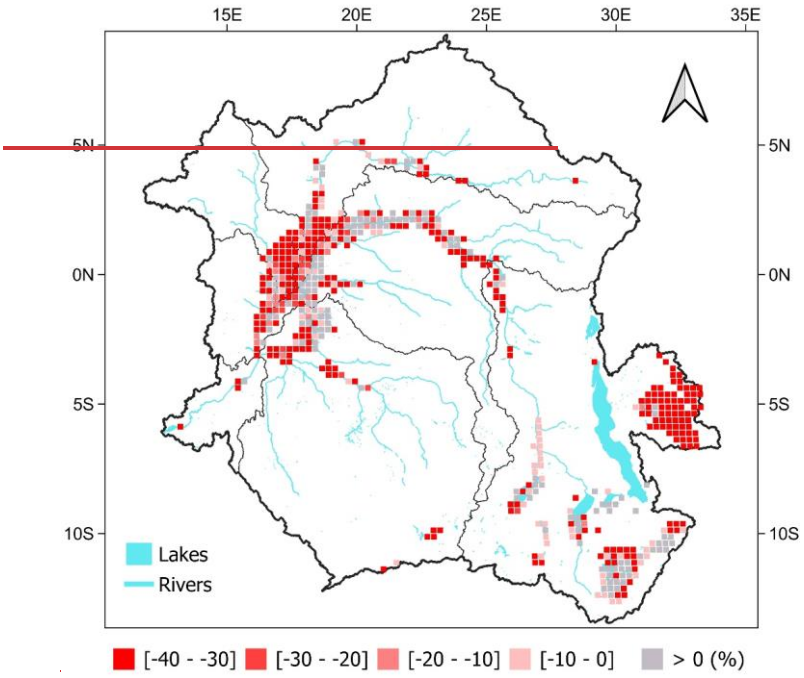

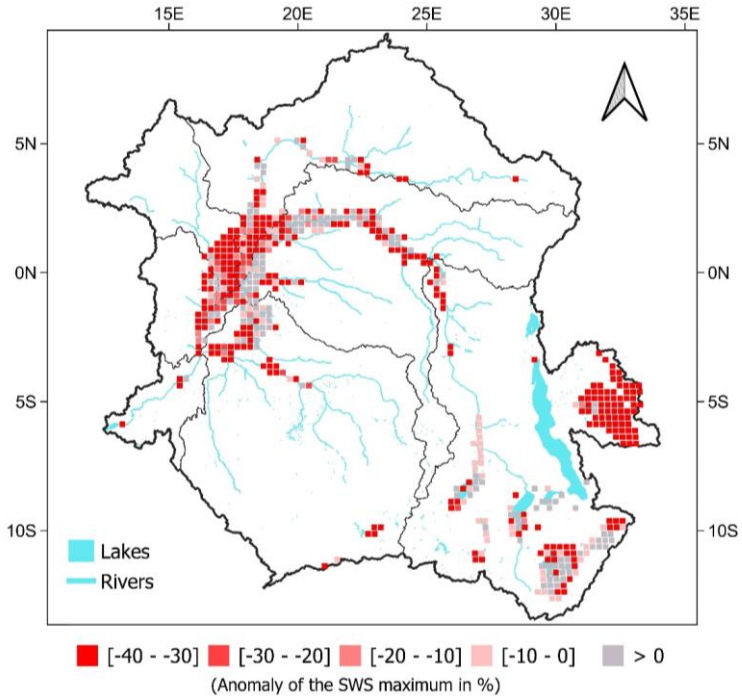

Figure 110: The 2005-2006 drought over the CRB as seen from the hypsometric curve approach SWS dataset based on FABDEM. Anomaly of the maximum SWS over November 2005 to January 2006 as compared to the 1992-2015 November-December-January mean value. The unit is in percentage of the 24-years mean monthly value.

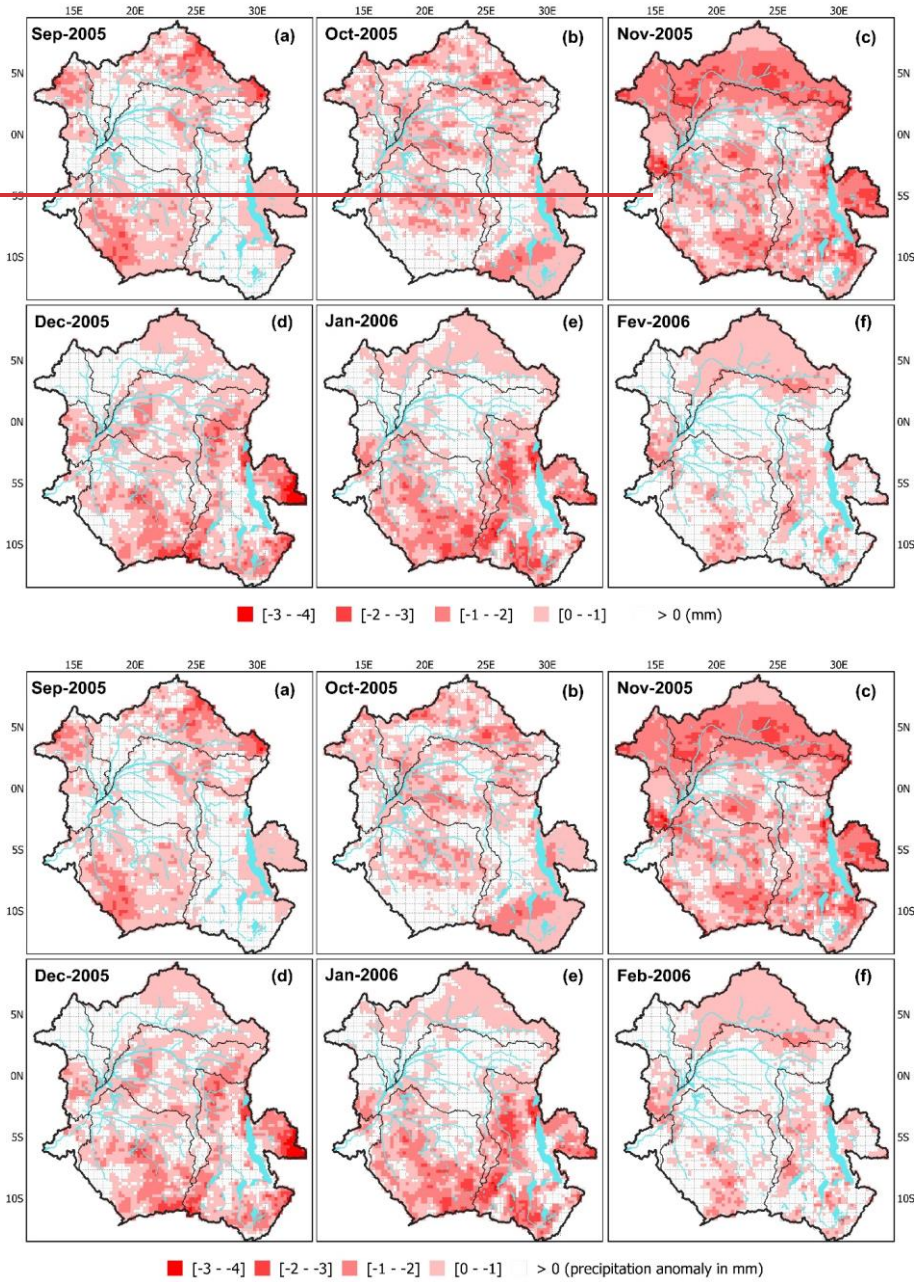

Figure 12~~1~~: Monthly mean spatial distribution of MSWEP precipitation anomaly in mm (resampled at 0.25° spatial resolution) from the period September 2005 to February 2006 based on the 1992-2015 climatology.

Table 1: Characteristics of the used Digital Elevation Models.

Dataset	**ALOS AW3D30**	**ASTER**	**MERIT**	**FABDEM**
Producer	JAXA Japan Aerospace Exploration Agency	NASA & METI National Aeronautics and Space Administration (US) Ministry of Economy, Trade, and Industry (Japan)	University of Tokyo	University of Bristol
Available at	https://www.eorc.jaxa.jp/ALOS/en/aw3d30/data/index.htm, last access: ~~0~~1 May~~November~~ 2023~~2~~	https://search.earthdata.nasa.gov/search/?fst0=Land%20Surface, last access: ~~0~~1 May~~November~~ 2023~~2~~	http://hydro.iis.u-tokyo.ac.jp/~yamadai/MERIT_DEM/, last access: ~~0~~1 May~~November~~ 2023~~2~~	https://doi.org/10.5523/bris.25wfy0f9ukoge2gs7a5mqpq2j7, last access: ~~0~~1 May~~November~~ 2023~~2~~
DEM coverage	90N-90S	83N-83S	90N-60S	80N-60S
Acquisition year	2006–2011	2000–2013	2000	2011–2015
Sensor	Panchromatic Remote-sensing Instrument for Stereo Mapping	Optical	AW3D30, Shuttle Radar Topography Mission (SRTM) & Viewfinder Panorama	Synthetic Aperture Radar (SAR) interferometer
Vertical datum	Orthometric EGM96	Orthometric EGM96	Orthometric EGM96	Orthometric EGM2008
Spatial resolution	30 m	30 m	90 m	30 m

Table 2: Location and main characteristics of the in situ discharge stations used in this study. The number in the first column refers to the location of the station in Fig. 1.

N°	**Name**	**Latitude**	**Longitude**	**Sub-basin**	**Period**	**Source**
1	Kisangani	0.51	25.19	Lualaba	1950-1959	CRREBaC
2	Bangui	4.37	18.61	Ubangui	1936-2020	CRREBaC/ SO-Hybam
3	Ouesso	1.62	16.07	Sangha	1947-2020	CRREBaC/ SO-Hybam
4	Lediba	-3.06	16.56	Kasaï	1950-1959	CRREBaC
5	Brazzaville/ Kinshasa	-4.3	15.30	Middle-Congo	1903-2020	CRREBaC/ SO-Hybam

Table 3: Mean annual amplitude over the CRB calculated from multi-satellite and hypsometric curve approaches. Error statistics comparing SWS from ALOS, ASTER, MERIT, and the multi-satellite approach against SWS from FABDEM, considered here as the reference. Comparisons are done over the same period by aggregating all SWS pixels over the basin for the compared datasets. MAE stands for mean absolute error and RMSE for root mean squared error, in km³.

Method	DEM	Time span	Mean annual amplitude (km³)	Error in relation to SWS from FABDEM (km³)	
				MAE	RMSE
Hypsometric curve approach	FABDEM	1992 - 2015	101 ± 23	/	/
	ALOS	1992 - 2015	80 ± 17	9	11
	ASTER	1992 - 2015	124 ± 25	22	26
	MERIT	1992 - 2015	80 ± 20	5	7
Multi-satellite approach	/	1995 - 2015	70 ± 17	18	22

Table 4: Summary of the maximum linear Pearson correlation coefficient r along with the lag for the comparison between SWS, precipitation, and discharge. Des. Ano. stands for deseasonalized anomalies. In bold are shown the significant correlation coefficients with p value < 0.01. For Kasaï and Lualaba sub-basins no contemporary discharge data are available therefore no correlation are reported.

Basin and sub-basin	r(lag)			
	SWS vs Precipitation		SWS vs Discharge	
	Raw series	Des. Ano.	Raw series	Des. Ano.
CRB	**0.56**(0)	**0.12(0)**	**0.57**(0)	**0.52**(0)
Sangha	0.04(0)	0.15(-2)	**0.73**(0)	**0.43**(0)
Ubangui	**0.63**(-2)	-0.06(3)	**0.89**(0)	**0.39**(0)
Middle-Congo	**0.32**(0)	0(3)	**0.87**(1)	**0.58**(1)
Kasaï	**0.69**(0)	0.03(-2)	/	/
Lualaba	**0.50**(0)	**0.43**(-2)	/	/